

[Click here to view linked References](#)

# 1 Shocked monazite chronometry: integrating microstructural and *in* 2 *situ* isotopic age data for determining precise impact ages

3 Timmons M. Erickson<sup>1</sup>, Nicholas E. Timms<sup>1</sup>, Christopher L Kirkland<sup>1</sup>, Eric Tohver<sup>2</sup>, Aaron J. Cavosie<sup>1, 3</sup>,  
4 Mark A. Pearce<sup>4</sup>, Steven M. Reddy<sup>1</sup>

5 1. TIGeR (The Institute of Geoscience Research), Dept. of Applied Geology, Curtin University, GPO  
6 Box 1984, Perth, WA, 6845, Australia

7 2. School of Earth and Environment, University of Western Australia, Perth, WA, 6009, Australia

8 3. NASA Astrobiology Institute, Department of Geoscience, University of Wisconsin-Madison,  
9 Madison WI, 53706, USA

10 4. CSIRO Mineral Resources, Australian Resources Research Centre, 26 Dick Perry Avenue,

11 Kensington, WA 6151, Australia

12 \*Corresponding Author: Timmons.Erickson@gmail.com

13 **Keywords:** Shock metamorphism, monazite, Araguainha, Vredefort, U-Pb geochronology, EBSD

## 14 Abstract

15 Monazite is a robust geochronometer and occurs in a wide range of rock types. Monazite  
16 also records shock deformation from meteorite impact but the effects of impact-related  
17 microstructures on the U – Th – Pb systematics remain poorly constrained. We have therefore  
18 analyzed shock-deformed monazite grains from the central uplift of the Vredefort impact structure,  
19 South Africa, and impact melt from the Araguainha impact structure, Brazil, using electron  
20 backscatter diffraction (EBSD), electron microprobe elemental mapping, and secondary ion mass  
21 spectrometry (SIMS). Crystallographic orientation mapping of monazite grains from both impact  
22 structures reveals a similar combination of crystal-plastic deformation features, including shock  
23 twins, planar deformation bands and neoblasts. Shock twins were documented in up to 4 different  
24 orientations within individual monazite grains, occurring as compound and/or type one twins in  
25 (001), (100), (10 $\bar{1}$ ), {110}, {212}, and type two (irrational) twin planes with rational shear directions  
26 in [0 $\bar{1}\bar{1}$ ] and [ $\bar{1}\bar{1}$ 0]. SIMS U – Th – Pb analyses of the plastically-deformed parent domains reveal

1  
2  
3  
4  
5  
6  
7  
8  
9  
10  
11  
12  
13  
14  
15  
16  
17  
18  
19  
20  
21  
22  
23  
24  
25  
26  
27  
28  
29  
30  
31  
32  
33  
34  
35  
36  
37  
38

discordant age arrays, where discordance scales with increasing plastic strain. The correlation between discordance and strain is likely a result of the formation of fast diffusion pathways during the shock event. Neoblasts in granular monazite domains are strain free, having grown during the impact events via consumption of strained parent grains. Neoblastic monazite from the Inlandsee leucogranofels at Vredefort records a  $^{207}\text{Pb}/^{206}\text{Pb}$  age of  $2010 \pm 15\text{Ma}$  ( $2\sigma$ ,  $n=9$ ), consistent with previous impact age estimates of 2020 Ma. Neoblastic monazite from Araguainha impact melt yield a Concordia age of  $259 \pm 5\text{Ma}$  ( $2\sigma$ ,  $n=7$ ), which is consistent with previous impact age estimates of  $255 \pm 3\text{Ma}$ . Our results demonstrate that targeting discrete microstructural domains in shocked monazite, as identified through orientation mapping, for *in situ* U – Th – Pb analysis can date impact-related deformation. Monazite is therefore one of the few high-temperature geochronometers that can be used for accurate and precise dating of meteorite impacts.

## 39 Introduction

40 Impact cratering is one of the most ubiquitous processes in the solar system (French and  
41 Koeberl 2010). Because terrestrial impact craters form basins that are subject to erosion, burial and  
42 destruction by plate tectonic activity, the record of meteorite impacts on Earth is incomplete, limited  
43 to 190 confirmed structures (Spray and Hines 2016). The majority of confirmed impact craters on  
44 Earth have poor age constraints due to the lack of suitable geochronometers (Jourdan et al. 2009;  
45 Jourdan et al. 2012). As a consequence, fundamental questions regarding the connections between  
46 impacts events and significant changes to both the lithosphere and biosphere remain unanswered.  
47 Shock deformation microstructures in minerals are one of a limited number of diagnostic criteria  
48 used to identify an impact event (French and Koeberl 2010). Crystal-plastic deformation caused by  
49 shock metamorphism has been shown to reset U-Th-Pb systems in some minerals to the time of  
50 impact (Moser et al. 2009; Moser et al. 2011; Cavosie et al. 2015a). It is therefore important to  
51 understand the effects of shock metamorphism on U – Th – Pb systematics to accurately date impact  
52 events (e.g. Moser et al. 2011).

53 Monazite,  $(La,Ce,Th)PO_4$ , is a common accessory phase that has been used as a tracer to study a  
54 variety of crustal processes due to the incorporation of U, Th, and other trace elements into its  
55 crystal structure (Catlos 2013). Even though shocked monazite has been reported from a few impact  
56 environments (e.g. Schärer and Deutsch 1990), recent advancements in electron backscatter  
57 diffraction (EBSD) mapping have permitted the systematic quantification of crystal-plastic  
58 deformation in monazite (e.g. Erickson et al. 2016a). However, the effects of specific impact-related  
59 deformation microstructures on the U – Th- Pb systematics in monazite have not been evaluated. In  
60 this study, we use EBSD to document shock microstructures in monazite from both the Vredefort  
61 Dome (South Africa) and Araguinha (Brazil) impact structures. Discrete domains were then targeted  
62 for secondary ion mass spectrometry (SIMS) analysis to understand what effects these features

63 have on the U-Th-Pb ages of shocked monazite, and to identify specific microstructures that yield  
64 accurate impact ages.

#### 65 **Shock deformation microstructures**

66 Meteorite impacts generate extremely high pressures (10s of GPa and greater) in target rocks  
67 over instantaneous time periods (ms – s; Melosh 1989). The passage of the shock front through the  
68 target and impactor creates unique microstructural deformation, such as high-pressure phases,  
69 planar microstructures, and twins (French and Koeberl 2010). Minerals with unique impact-related  
70 deformation are commonly referred to as shocked minerals (Langenhorst and Deutsch 2012). The  
71 conditions required to develop shock deformation features vary with host mineral, and are best  
72 constrained for quartz. Quartz develops multiple sets of crystallographically-controlled lamellae  
73 called planar deformation features (PDF) that form between 10 and 34 GPa. At higher pressures,  
74 quartz transforms to diaplectic SiO<sub>2</sub>, which may revert to stishovite or coesite during release of the  
75 shock pressures (Stöffler and Langenhorst 1994). Of common accessory phases, zircon has the most  
76 well-constrained impact-related microstructures, which develop by 20 GPa (Leroux et al. 1999).  
77 Deformation twins are ubiquitous in shocked zircon, and have been observed in both static diamond  
78 anvil cell experiments at 20 GPa (Morozova 2015) and a variety of impact environments (e.g. Moser  
79 et al. 2011; Timms et al. 2012; Erickson et al. 2013a). At higher pressure, zircon transforms to the  
80 high pressure polymorph reidite (Leroux et al. 1999; Wittmann et al. 2006; Reddy et al. 2015;  
81 Cavosie et al. 2015b; Erickson et al. 2017), which occurs at or above 30 GPa in shock experiments  
82 (Kusaba et al. 1985; Leroux et al. 1999). At more extreme shock conditions, zircon can develop  
83 granular texture (Bohor et al. 1993; Wittmann et al. 2006; Cavosie et al. 2015a; Cavosie et al. 2016;  
84 Timms et al. 2017). Granular zircon with systematic misorientations of 90°/⟨110⟩ and 65°/⟨110⟩  
85 likely result from recrystallization of reidite and zircon {112} twins, respectively, and can contain  
86 evidence of partial dissociation to ZrO<sub>2</sub> that requires extreme temperature excursions due to the  
87 impact event (Cavosie et al. 2016; Timms et al. 2017).

#### 88 **Deformation microstructures in monazite**



89 A range of deformation-related microstructures have been reported in monazite, including  
1  
2 90 mechanical twinning, lattice strain, and recrystallization. Monazite deformation twins in (100), (001),  
3  
4 91 {120} and {12 $\bar{2}$ } have been produced in indentation experiments at ambient temperature and  
5  
6 92 pressure and imaged by transmission electron microscopy (TEM) (Hay and Marshall 2003). In  
7  
8 93 tectonically deformed monazite, mechanical twins, crystal-plastic strain, and dynamically-  
9  
10 94 recrystallized neoblasts were identified by EBSD (Erickson et al. 2015). Crystal-plastic deformation,  
11  
12 95 including low-angle (<10°) subgrain boundaries, was predominantly accomplished by slip systems  
13  
14 96 which result in disorientations about <010> and <101>, and sets of deformation twins were found in  
15  
16 97 (100), (001), and {12 $\bar{2}$ } (Erickson et al. 2015), which are the same twin orientations found in  
17  
18 98 experimental studies (Hay and Marshall 2003). In the tectonically deformed monazite grains, strain-  
19  
20 99 free neoblasts nucleated within high-strain domains and consumed the parent monazite by grain  
21  
22 100 boundary migration (Erickson et al. 2015). Within the deformed monazite, the U – Th – Pb  
23  
24 101 systematics were disturbed and variable age resetting was shown to correlate with plastic strain; the  
25  
26 102 authors interpreted that Pb-loss was facilitated by formation of fast diffusion pathways during  
27  
28 103 deformation (Erickson et al. 2015). Nucleation and growth of neoblastic monazite was driven by  
29  
30 104 strain energy within the deformed lattice. Neoblasts excluded inherited Pb, and record  
31  
32 105 Neoproterozoic U – Pb ages consistent with the age of regional tectonometamorphism (Buick et al.  
33  
34 106 2010; Erickson et al. 2015).

42 107 Naturally-shocked monazite with planar fractures was first reported from the ca. 39 Ma, 23 km  
43  
44 108 diameter, Haughton impact structure, Canada (Schärer and Deutsch 1990). Shock-deformed  
45  
46 109 monazite with planar microstructures and granular textures have since been described in bedrock  
47  
48 110 from the Vredefort Dome, South Africa (Moser 1997; Hart et al. 1999; Flowers et al. 2003) and the  
49  
50 111 Araguinha impact crater, Brazil (Tohver et al. 2012; Silva et al. 2016). Most prior studies  
51  
52 112 documented microstructures using BSE images, however lattice strain in the above examples have  
53  
54 113 not be quantitatively characterized.  
55  
56  
57  
58  
59  
60  
61  
62  
63  
64  
65

114 In addition to occurrences in bedrock, shocked monazite has also been identified in detrital  
115 populations derived from the Vredefort Dome (Cavosie et al. 2010; Erickson et al. 2013b; Cavosie et  
116 al. in press). Monazite grains containing planar features were found within the Vaal River and its  
117 tributaries, which cross-cut the Vredefort Dome (Cavosie et al. 2010), at sites up to 750 km  
118 downriver (Erickson et al. 2013b), and in Pleistocene fluvial terraces of the Vaal River (Cavosie et al.  
119 in press). Microstructural analysis of detrital shocked monazite by EBSD (Erickson et al. 2016a)  
120 identified a variety of deformation microstructures including sets of twins in up to 10 different  
121 orientations, planar deformation bands (PDBs) and neoblasts. Seven twin relationships were  
122 documented in the detrital shock monazite grains that have not been observed in tectonically-  
123 deformed grains; these features have been attributed to shock deformation, and occur along with  
124 the twin types reported in tectonically-deformed monazite (100), (001), and  $\{12\bar{2}\}$  (Erickson et al.  
125 2016a). Critically, the detrital shocked monazite grains contain zircon inclusions exhibiting  $\{112\}$   
126 twins that require minimum shock pressures of 20 GPa, thus providing an empirical constraint on the  
127 shock features in the host monazite grains. Erickson et al. (2016a) interpreted that the seven  
128 previously unreported twin orientations, including  $(10\bar{1})$ ,  $\{\bar{1}10\}$ ,  $(10\bar{2})$ ,  $\{212\}$ ,  $\{\bar{1}\bar{2}0\}$ , and two  
129 irrational planes containing shear directions ( $\eta_1$ ) in  $[01\bar{1}]$  and  $[\bar{1}\bar{1}0]$  represent *bona fide* shock  
130 microstructures.

131 Several studies have addressed aspects of experimental shock deformation on microstructural  
132 and isotopic systematics of monazite. An experimental study by Deutsch and Schärer (1990) tested  
133 the effects of shock metamorphism on the U – Pb systematics by subjecting a monazite crystal to 59  
134 GPa and temperatures  $>1200$  °C followed by rapid cooling. While the experiment yielded monazite  
135 with significantly lower birefringence, intense mosaicism and sub-parallel fractures (Deutsch and  
136 Schärer 1990; their Fig. 3b), the authors found no significant disturbance to the U – Pb isotopic  
137 system. It has been noted that shock experiments may not represent the full range of shock  
138 deformation features found in nature (Deutsch and Schärer 1990; Niihara et al. 2012), given the  
139 time-scales of experiments are orders-of-magnitude shorter than natural impact events. Other

140 studies have analyzed the effects of the high-pressure shock wave caused by plasma expansion  
141 during femtosecond laser ablation analysis of monazite (Seydoux-Guillaume et al. 2010; D'Abzac et  
142 al. 2012). Microstructural features observed within the region directly adjacent to the laser ablation  
143 pit include deformation twinning, crystal-plasticity, mosaicism and the formation of micron-scale  
144 granules (Seydoux-Guillaume et al. 2010; D'Abzac et al. 2012).

145 Naturally shocked monazite grains with planar microstructures from Vredefort bedrock (Flowers  
146 et al. 2003) and detritus (Erickson et al. 2013b) were found to record pre-impact ages when analyzed  
147 by thermal ionization mass spectrometry (TIMS) and SIMS, respectively. However, monazite that has  
148 recrystallized during shocked metamorphism and yields impact ages has been reported at both the  
149 Vredefort Dome (Moser 1997) and Araguinha structures (Tohver et al. 2012). Because deformation  
150 can variably reset the U – Pb systematics in monazite (Wawrzenitz et al. 2012; Erickson et al. 2015;  
151 Erickson et al. 2016b), shock-deformed monazite may be a valuable impact chronometer. In this  
152 study, we analyzed monazite and zircon from the inlandsee leucogranofels located in the central  
153 uplift of the Vredefort Dome and in impact melt from the Araguinha impact structure. The aim of  
154 this study is three-fold: firstly, to systematically characterize shock microstructures in monazite from  
155 these impact craters to compare shocked monazite from different impact environments ; secondly,  
156 constrain the shock conditions experienced by monazite through analysis of deformation  
157 microstructures in zircon from the same samples; thirdly, to quantify the effects of shock  
158 deformation on U – Th – Pb ages in monazite with well-characterized microstructures from impact  
159 craters where the impact age has been independently constrained in order to rigorously evaluate  
160 the application of shocked monazite as an impact chronometer.

## 161 **Geologic background and samples**

### 162 ***Vredefort impact structure, South Africa***

163 The Vredefort impact structure is a ca. 2020 Ma deeply eroded crater located within the  
164 Kaapvaal Craton in South Africa (Kamo et al. 1996; Gibson et al. 1997; Moser 1997). The Vredefort

165 Dome is the ~ 90 km diameter erosional remains of the central uplift of the complex crater. The  
166 central uplift contains a complex internal structure consisting of a 40 km diameter inner core,  
167 comprised of the granulite facies Inlandsee leucogranofels (ILG) and the amphibolite facies Outer  
168 Granite Gneiss, and an outer collar which consists of a ~ 25 km thick ring of over-turned Archean and  
169 Paleoproterozoic metasedimentary and metavolcanic rocks (Fig. 1 a; Bischoff et al. 1999). The outer  
170 ring creates a topographic high around the weathered granitoids and gneisses, from which the upper  
171 8 – 11 km have been removed (Gibson et al. 1998). Modeling of mineral indicators of impact  
172 pressures within the Vredefort Dome and structural studies of the surrounding Witwatersrand basin  
173 suggests that the transient crater was between 200 and 300 km wide (Ivanov 2005) and contained  
174 the entire Witwatersrand basin. The Vredefort Dome experienced post-impact, low-grade,  
175 metamorphism associated with emplacement of mafic intrusions at ca. 1000 Ma (Reimold et al.  
176 2000), which may have resulted in Pb-loss within some zircon grains at this time (Moser et al. 2011).

177         The core of the Vredefort Dome is comprised of 3420 to 3000 Ma Archean granitoids,  
178 charnockitic gneiss, and supracrustal rocks metamorphosed at high regional grades in the Archean  
179 (Hart et al. 1999; Moser et al. 2001; Armstrong et al. 2006) that subsequently experienced pyroxene-  
180 hornfels metamorphism during the impact, where temperatures locally reached as high as 1300 °C  
181 (Gibson 2002). Three occurrences of shocked monazite have been reported from Vredefort bedrock  
182 (Fig. 1 a; Moser 1997; Hart et al. 1999; Flowers et al. 2003). Shocked monazite that record pre-  
183 impact ages with partial Pb-loss were reported by Hart et al. (1999) from a granulite-facies  
184 garnetiferous paragneiss, near the center of the Vredefort Dome. Shocked monazite with cross-  
185 cutting planar microstructures within gneissic quartz monzonite near the granulite-amphibolite  
186 transition within the Vredefort Dome was dated by ID-TIMS by (Flowers et al. 2003). The U – Th – Pb  
187 analysis documented partial Pb-loss, defining an age array from 3180 Ma to 2260 Ma. The authors  
188 interpreted upper intercepts to represent regional metamorphism associated with intrusions  
189 between 3130 and 3080 Ma (Flowers et al. 2003).

190 Monazite with granular texture from the ILG, located at the center of the Vredefort Dome,  
1 record complete isotopic age resetting (Moser 1997). The ILG (Stephens 1990) is composed of a  
2  
3  
4  
5 192 sequence of felsic high-grade metamorphosed, migmatitic Archean TTG, enderbite and charnockite  
6  
7 193 (Flowers et al. 2003), all thermally recrystallized by the shock event (Gibson and Reimold 2005). Two  
8  
9 194 granular monazite grains dated by ID-TIMS (Moser 1997) yielded  $^{207}\text{Pb}/^{206}\text{Pb}$  ages of  $2090 \pm 4$  ( $2\sigma$ ),  
10  
11 195 and  $2016 \pm 7$  ( $2\sigma$ ), the latter of which is within error of impact-generated zircon at Vredefort (Kamo  
12  
13 196 et al. 1996; Gibson et al. 1997; Moser 1997). Zircon from the same ILG sample yielded a discordant  
14  
15  
16 197 U – Pb array, with an upper intercept of 3290 Ma and lower intercept of ca. 2020 Ma (Moser 1997).  
17  
18 198 Moser et al. (2011) analyzed shocked zircon from the ILG using EBSD. The authors identified low-  
19  
20  
21 199 angle boundaries, shock twins and sub-planar fractures (Moser et al. 2011). U – Pb SIMS analysis of  
22  
23 200 the ILG zircon displayed a discordant array, from which three of four analyses spread between  $3471$   
24  
25  
26 201  $\pm 61$  Ma and 2020 Ma (Moser et al. 2011). A sample of ILG foliated felsic gneiss, 09SA06 (Fig. 1 a),  
27  
28 202 was selected for analysis by EBSD and SIMS because monazite grains reported from the ILG show  
29  
30  
31 203 significant recrystallization textures (Moser 1997), the zircon grains preserve shock twinning and  
32  
33 204 plastic deformation (Moser et al. 2011), and variable resetting of the U – Th – Pb systems was  
34  
35 205 detected between the two phases.  
36

### 37 38 206 **Araguainha impact structure, Brazil**

39  
40 207 The ca. 255 Ma Araguainha impact structure is a ~40 km diameter complex crater located  
41  
42 208 within the Paraná Basin of central Brazil (Tohver et al. 2012). The impact punctured 1500 – 1800 m  
43  
44 209 thick Permian to Devonian stratigraphy of the Paraná Basin, exposing Cambrian granitic basement  
45  
46  
47 210 within the ~ 5 km diameter central uplift (Fig. 1 b; Lana et al. 2007; Lana et al. 2008; Tohver et al.  
48  
49 211 2012). The Araguainha granite is a pink, coarse grained monzo-syenogranite, with a crystallization  
50  
51 212 age of  $510 \pm 12$  Ma (Tohver et al. 2012). The granite is cross-cut by an impact melt-bearing,  
52  
53  
54 213 polymictic breccia, or suevite (Engelhardt et al. 1992), dominantly derived from the local granite  
55  
56 214 (Machado et al. 2009; Tohver et al. 2012).  
57  
58  
59  
60  
61  
62  
63  
64  
65

215 Shock-deformed monazite grains have been identified within shocked Araguainha granite,  
1 partially melted granite, suevite, and within melt sheet/veins in the central uplift (Tohver et al. 2012;  
2 216 Silva et al. 2016). Monazite grains from shocked granite show cross-cutting, double-walled, planar  
3  
4 217 features (Silva et al. 2016), that appear consistent with shock twins reported elsewhere (cf. Erickson  
5  
6 218 et al. 2016a). In partially melted granite monazite grains show an annealed texture, consistent with  
7  
8 219 dynamic recrystallization (Silva et al. 2016). Within Araguainha impact melt, Silva et al. (2016)  
9  
10 220 identified multiple textures within the monazite grains, including planar features, annealed  
11  
12 221 polycrystalline aggregates, and a distinctive cataclastic microstructure.  
13  
14  
15  
16  
17

18  
19 223 Two types of shock features were identified within monazite from the impact melt rock of  
20  
21 224 Tohver et al. (2012), including planar fractures and ‘granular aggregates’. Planar fractures display  
22  
23 225 trails of inclusions cross-cutting the monazite in polished section, while aggregates of  
24  
25 226 ‘neocrystallized’ monazite granules display curved boundaries and form triple junctions (Tohver et  
26  
27 227 al. 2012; their Fig. 6). Shocked monazite grains were dated by Tohver et al. (2012) and show a  
28  
29 228 bimodal age distribution, with ages spread between ca. 500 and 250 Ma, which the authors  
30  
31 229 interpreted as representing both inherited deformed monazite and impact-generated recrystallized  
32  
33 230 monazite. Domains containing planar microstructure record the oldest ages, which range from ca.  
34  
35 231 498 Ma to ca. 350 Ma. The population of monazite made up of aggregates of neocrystalline granules  
36  
37 232 record an U – Th – Pb age of  $255 \pm 3$  Ma, which the authors interpreted as the age of the Araguainha  
38  
39 233 impact (Tohver et al. 2012). Due to the complex microstructures exhibited by the shocked monazite  
40  
41 234 from Araguainha impact melt (AIM) sample of Tohver et al. (2012) and their bimodal age  
42  
43 235 distribution, we selected this sample for EBSD and further SIMS analysis.  
44  
45  
46  
47  
48  
49

## 50 236 **Methods**

51  
52  
53 237 Monazite and zircon were separated from ILG sample 09SA06 (27° 2.870' S, 27° 29.603' E)  
54  
55 238 and from AIM sample ARA (16° 49.329' S, 53° 0.150' W) of Tohver et al. (2012). Monazite and zircon  
56  
57 239 were analyzed by EBSD using previously established approaches (Reddy et al. 2007; Erickson et al.  
58  
59  
60  
61  
62  
63  
64  
65

240 2015). Scanning electron microscopy, including EBSD analysis, was undertaken with a Tescan Mira3  
241 Field emission gun scanning electron microscope within the John de Laeter Centre (JDLC) at Curtin  
242 University. For further details on the methodologies see Appendix 1. Additional EBSD maps for  
243 zircon and monazite from 09SA06 and ARA can be found in appendices 2 – 5, respectively. U – Th –  
244 Pb SIMS analysis of shocked monazite grains were undertaken with a SHRIMP II housed within the  
245 JDLC after the methods of (Fletcher et al. 2010); see appendix 1 for more details. The cumulative  
246 plastic misorientation within each SIMS analytical domain were calculated from the equivalent  
247 region of the EBSD maps (e.g. Figs. 2c and 4c) as the grain orientation spread (GOS and GOS avg.); for  
248 further details on this calculation see Appendix 1. Element maps of monazite grains were acquired  
249 using a Cameca SXFive electron probe microanalyzer (EPMA) at Adelaide Microscopy at the  
250 University of Adelaide (see Appendix 1).

## 251 **Results**

252 Orientation maps of eight monazite and four zircon grains from sample 09SA06 from the  
253 Vredefort ILG were made using EBSD. An additional 11 monazite and three zircon grains were  
254 analyzed from sample ARA from the Araguainha impact melt. Monazite and zircon microstructures  
255 are summarized below. In addition, U – Th – Pb analyses targeting specific microstructural domains  
256 for monazite grains from both samples are reported in Tables 1 & 2.

### 257 **Vredefort ILG- monazite microstructures**

258 Monazite grains from the ILG contain multiple types of microstructure, including crystal-  
259 plastic strain, deformation twinning and randomly-oriented, low-strain subdomains. The grains are  
260 variably complex, from being dominated by crystal-plastic strain with a combination of low-angle  
261 boundaries and deformation twins (e.g. Grain 8, Fig. 2), to dominated by randomly-oriented  
262 subdomains (e.g. Grain 3, Fig. 2), or a combination of both microstructural types (e.g. Grain 7, Fig. 2).  
263 Four monazite grains contain deformation twins, which occur in up to two orientations per grain,  
264 with the following minimum misorientation relationships (as angle/axis pairs) from the host grain;

1 265  $180^\circ / \langle 101 \rangle$ ,  $95^\circ / \langle 201 \rangle$  and  $150^\circ / \langle 10\bar{1} \rangle$ , which are consistent with twins in  $(10\bar{1})$ ,  $\{1\bar{2}\bar{2}\}$  and  
2 266  $\{212\}$ , respectively (Erickson et al. 2016a). Grain 3 is composed entirely of strain-free subdomains,  
3  
4 267 which range between  $68.6 \mu\text{m}$  and  $1.7 \mu\text{m}$  diameter (mean =  $17.5 \mu\text{m}$ ). Elemental maps for Th reveal  
5  
6 268 complex zonation textures; within the high strain domains, the grains preserve both concentric  
7  
8 269 (grain 8) or patchy zonation (grain 7), while some of the strain free subdomains preserve sector  
9  
10 270 zoning patterns (grain 3, Fig. 2 d).  
11  
12

13 271 The eight ILG monazite grains contain a variety of intergrowths and/or inclusions, including  
14  
15 272 both zircon (2 of 8) and apatite (5 of 8) grains. The apatite inclusions occur within both crystal-  
16  
17 273 plastically strained domains (e.g. grain 1, appendix 2) and within low-strain subdomains (e.g. grain 3,  
18  
19 274 Fig. 2) of the monazite grains, and therefore predate shock deformation. Two monazite grains also  
20  
21 275 contain zircon inclusions (grains 1, 4, appendix 2), which record minor degrees of crystal-plastic  
22  
23 276 strain, but no features diagnostic of shock deformation (cf., Erickson et al. 2016a).  
24  
25  
26  
27

#### 28 277 **Vredefort ILG- zircon microstructures**

29  
30 278 Cathodoluminescence (CL) images of zircon from the ILG reveal dark, concentric zoned  
31  
32 279 cores, and bright sector zoned rims (Fig. 3a). Lamellae that are bright in CL also cross-cut growth  
33  
34 280 zoning, which is especially evident in the CL dark cores. All four zircon grains mapped by EBSD  
35  
36 281 contain twin lamellae that are misoriented  $65^\circ / \langle 110 \rangle$  with the host grain, and align with the bright  
37  
38 282 CL lamellae (appendix 3). However, the localized bright CL sections of some lamellae are in the  
39  
40 283 crystallographic orientation of the parent grain, rather than preserving a twin orientation (Figs. 2 a,  
41  
42 284 c).  
43  
44  
45  
46

#### 47 285 **Araguainha impact melt- monazite microstructures**

48  
49 286 Shock-deformed monazite grains within the AIM contain similar microstructures to the ILG  
50  
51 287 monazite, including crystal-plastic strain, deformation twinning and strain-free domains. Of eleven  
52  
53 288 grains analyzed by EBSD, all contain crystal-plastically strained domains with sub-planar low-angle  
54  
55 289 boundaries (e.g. grains 10, 11, Fig. 4). The grains each contain between 1 and 4 sets of deformation  
56  
57 290 twins with the following minimum misorientation relationships;  $180^\circ / \langle 100 \rangle$ ,  $180^\circ / \langle 001 \rangle$ ,  $180^\circ /$   
58  
59  
60  
61  
62  
63  
64  
65



291  $\langle 101 \rangle$ ,  $94^\circ / \langle 001 \rangle$ ,  $150^\circ / \langle 10\bar{1} \rangle$ ,  $85^\circ / \langle 401 \rangle$  and  $91^\circ / \langle 104 \rangle$ . The twins are consistent with  
292 known monazite twin orientations observed at the Vredefort Dome; compound twin planes in (001),  
293 (100),  $(10\bar{1})$ , type 1 (rational) twin planes in  $\{110\}$ ,  $\{212\}$  and type two (irrational) twin planes with  
294 rational shear directions ( $\eta_1$ ) in  $[0\bar{1}\bar{1}]$  and  $[\bar{1}\bar{1}0]$ , respectively (Erickson et al. 2016a). Many shock  
295 twins are discontinuous, and have irregular, non-planar interfaces but fall along linear traces (Fig. 5  
296 b). Ten of the eleven monazite grains also contain strain-free domains, which are randomly-oriented  
297 relative to the strained parent grains, and range in diameter between 24.5 and 1.0  $\mu\text{m}$ , with a mean  
298 diameter of 8.0  $\mu\text{m}$  (Figs. 4, 5). Elemental maps of Th reveal concentric or sector zonation patterns,  
299 which are moderately overprinted by a patchy texture (Fig. 4 d). In grain 10, the strain-free,  
300 randomly-oriented domains, correspond with the zone of highest Th concentrations in the grain,  
301 however other grains do not show this pattern. Only one of the analyzed shocked monazite grains  
302 from Araguinha contains a zircon inclusion ( $\sim 10 \mu\text{m}$ ), which preserves a polycrystalline  
303 microstructure (granular texture) similar to that described in Cavosie et al. (2016).

#### 304 **Araguinha impact melt- zircon microstructures**

305 Three shocked zircon grains from the AIM contain a variety of both crystal-plastic and  
306 recrystallization textures. The zircon grains contain  $\{100\}$  PDBs, a  $\{112\}$  twin lamella in one grain,  
307 and granular texture (appendix 5). The most complex zircon analyzed (Fig. 6) contains a crystal-  
308 plastically strained parent grain and misoriented subdomains. The subdomains include areas that are  
309 systematically misoriented from the parent grain with  $65^\circ / \langle 110 \rangle$  or  $90^\circ / \langle 110 \rangle$  relationships, and  
310 also neoblasts that are randomly oriented (Figs. 6 b – e). The neoblasts range between 1.0 and 6.9  
311  $\mu\text{m}$  in diameter (mean equivalent circle diameter = 1.8  $\mu\text{m}$ ).

#### 312 **Monazite in situ U – Th – Pb geochronology**

313 A total of 19 SIMS analyses were collected from three monazite grains from the ILG sample  
314 09SA06; seven analyses from grain 3, six from grain 7 and six from grain 8. Eight analyses were  
315 obtained from crystal-plastically strained domains in grains 7 and 8, while eleven were acquired  
316 from low-strain subdomains (Grain orientation spread, GOS Avg.,  $< 0.9^\circ$ ) in all three grains (Fig. 2 b).

1  
2 317 Apparent ages from ILG monazite show a bimodal age distribution (Fig. 7 a). Analytical spots from  
3  
4 318 the strained host are variably discordant ( $> 10\%$  between  $^{206}\text{Pb}/^{207}\text{Pb}$  and  $^{206}\text{Pb}/^{238}\text{U}$ ), with apparent  
5  
6 319  $^{207}\text{Pb}/^{206}\text{Pb}$  ages between  $2537 \pm 26$  Ma and  $2386 \pm 26$  Ma ( $2\sigma$ ). Spots from the low-strain, randomly-  
7  
8 320 oriented subdomains show a tight cluster around concordia and are all  $< 9\%$  discordant, with  
9  
10 321  $^{207}\text{Pb}/^{206}\text{Pb}$  ages ranging between 2102 and 1987 Ma (Fig. 7 b). The analyses show a relationship  
11  
12 322 between U-Th discordance and common Pb as estimated based on measured  $^{204}\text{Pb}$  (Fig. 7 b).  
13  
14 323 Nevertheless, the 9 most concordant analyses, (all  $< 7.5\%$  discordant) yield a weighted mean  
15  
16 324  $^{207}\text{Pb}/^{206}\text{Pb}$  date of  $2010 \pm 15$  ( $2\sigma$ ,  $n=9$ ,  $\text{MSWD} = 0.84$ ).

17  
18  
19 325 A total of 14 SIMS analyses were collected from two monazite grains from the Araguainha  
20  
21 326 impact melt rock, ARA. Four spots were collected from grain 10 and ten spots from grain 11. Of the  
22  
23 327 fourteen analytical spots, seven were acquired from crystal-plastically strained domains and 7 were  
24  
25 328 acquired from strain-free (Grain orientation spread, GOS,  $< 0.3^\circ$ ) subdomains (Figs. 8 a – b). The data  
26  
27 329 define a bimodal age distribution along concordia. Plastically strained domains have apparent  
28  
29 330  $^{206}\text{Pb}/^{238}\text{U}$  ages ranging from  $467 \pm 12$  Ma to  $278 \pm 14$  Ma, with the 3 oldest ages originating from the  
30  
31 331 least strained portions of the parent grains (Fig. 8). Seven analyses from strain-free subdomains are  
32  
33 332 clustered on concordia ( $< 8\%$  discordance between  $^{208}\text{Pb}/^{232}\text{Th}$  and  $^{206}\text{Pb}/^{238}\text{U}$ ) and yield  $^{206}\text{Pb}/^{238}\text{U}$   
34  
35 333 ages between 265 Ma and 247 Ma (Fig. 8). Analyses from strain-free subdomains yield a concordia  
36  
37 334 age of  $259 \pm 5$  Ma ( $2\sigma$ ,  $n=7$ ,  $\text{MSWD} = 1.3$ ). However, if the analyses from grain 11, which contained  
38  
39 335 less common Pb and better agreement between the U – Th systematics than those from grain 10,  
40  
41 336 are solely considered, they yield a concordia age of  $262 \pm 3$  ( $2\sigma$ ,  $n=5$ ,  $\text{MSWD} = 0.88$ ).

## 42 337 Discussion

### 43 338 Impact-related microstructures in monazite: Twinning, PDBs, neoblasts

44  
45 339 In both samples, monazite grains contain a combination of domains which are crystal-  
46  
47 340 plastically strained, and domains that are randomly oriented and strain-free. The crystal-plastically  
48  
49 341 strained domains preserve a combination of cumulative strain across the grain accommodated by

1  
2  
3  
4  
5  
6  
7  
8  
9  
10  
11  
12  
13  
14  
15  
16  
17  
18  
19  
20  
21  
22  
23  
24  
25  
26  
27  
28  
29  
30  
31  
32  
33  
34  
35  
36  
37  
38  
39  
40  
41  
42  
43  
44  
45  
46  
47  
48  
49  
50  
51  
52  
53  
54  
55  
56  
57  
58  
59  
60  
61  
62  
63  
64  
65

342 low-angle grain boundaries, consistent with dislocation creep. The presence of deformation twins in  
343 strained domains from both samples is further evidence for crystal-plastic deformation. Twins found  
344 in both samples, including  $(10\bar{1})$  and  $\{212\}$  in the ILG monazite, and  $(10\bar{1})$ ,  $\{110\}$ ,  $\{212\}$ , and two  
345 type two (irrational) twin planes (with rational shear directions ( $\eta_1$ ) in  $[0\bar{1}\bar{1}]$  and  $[\bar{1}\bar{1}0]$ ) in the  
346 Araguinha grains, are diagnostic of shock metamorphism (Erickson et al. 2016a). The difference in  
347 shock-twin types and abundances between the ILG and the AIM monazite grains may be a result of  
348 variable shock environments; further work is required to constrain the conditions of formation for  
349 specific twin orientations in monazite.

350 Monazite grains from Araguinha impact melt contain abundant planar microstructures  
351 composed of low-angle boundaries that accommodate as much as  $11^\circ$  of misorientation (e.g.  
352 Araguinha grain 7, appendix 4). The planar microstructures are consistent with PDBs described in  
353 detrital shocked monazite derived from the Vredefort Dome (Erickson et al. 2016a). In addition to  
354 PDBs, the AIM monazite grains contain sub-planar, low-angle boundary microstructures, along which  
355 occur trails of non-indexing (by EBSD), lower atomic number material that is darker in BSE images  
356 (e.g. Fig. 5a). The sub-planar trails appear similar to features described in zircon from the Vredefort  
357 Dome by Moser et al. (2011), which the authors interpreted as channels of injected melt.

358 Monazite from both the ILG and the AIM contain randomly-oriented subdomains which are  
359 either low-strain (ILG) or strain-free (AIM) and are highly misoriented relative to the host grain. We  
360 interpret these as neoblastic monazite formed by recrystallization (Erickson et al. 2015). Monazite  
361 neoblasts nucleate on deformation features, such as grain boundaries, within the strained parent  
362 monazite, indicating that stored strain energy has a key role in effectively lowering energy required  
363 to overcome the energy barrier for nucleation and growth of new grains via grain boundary  
364 migration. Through this process, newly grown, strain-free monazite grains are bounded by high-  
365 angle grain boundaries relative to parent monazite. In addition, many of the neoblasts share specific  
366 crystallographic misorientation relationships with the host monazite that are consistent with known  
367 twin orientations for monazite (e.g. Figs. 4, 5a). The systematic orientations of monazite neoblasts,

1 368 therefore, suggest that monazite neoblasts preferentially nucleate in orientations that minimize the  
2 369 host-neoblast interfacial energy, including syntaxially from pre-existing twins and host orientations.  
3  
4 370 The formation of monazite neoblasts by dynamic recrystallization is not unique to shock  
5  
6 371 metamorphism; similar neoblastic monazite has been shown to form in deformed rocks from the  
7  
8 372 lower crust, in which, deformation occurs at high temperatures (Erickson et al. 2015). This process  
9  
10 373 forms new monazite, free of inherited Pb, that can be used to date high temperature deformation of  
11  
12 374 the lower crust (Erickson et al. 2015).

13  
14 375 We interpret the formation mechanism of neoblastic monazite during impact events to be  
15  
16 376 similar to those in tectonic settings, and may not require hypervelocity shock pressures. The process  
17  
18 377 of cannibalization of the host grain requires both strained lattice (as a result of shock) and high  
19  
20 378 temperature to facilitate neoblast nucleation and growth, conditions present immediately after  
21  
22 379 dissipation of the shock wave while post-shock temperatures are high. Monazite from the ILG  
23  
24 380 experienced post-shock temperatures as high as 1300 °C (Gibson 2002). Monazite grains from  
25  
26 381 Araguainha were entrained within impact melt; while the formation temperature is unconstrained,  
27  
28 382 at minimum, it would have been above the Araguainha granite liquidus (i.e., >700 °C), and likely  
29  
30 383 much hotter, because impact melts can be superheated and reach temperatures >2000 °C (Grieve et  
31  
32 384 al. 1977; Timms et al. 2017). Cooling rates from high-post shock temperatures are anticipated to  
33  
34 385 occur over timescales within uncertainty of quantitative *in situ* SIMS U – Th – Pb dating, and  
35  
36 386 therefore, the conditions which form neoblasts can be considered to be contemporaneous with  
37  
38 387 impact shock events.

#### 39 388 **Constraints on shock conditions**

40  
41 389 Analysis of shock microstructures within zircon from the two samples allows evaluation of the  
42  
43 390 P – T conditions experienced by shocked monazite (e.g. Erickson et al. 2016a). In the case of the ILG,  
44  
45 391 the post-shock > 1000 °C thermal pulse associated with granofels metamorphism (Gibson 2002), has  
46  
47 392 erased the shock features in many of the major phases (e.g. PDFs in quartz); however it has been  
48  
49 393 estimated that the central part of the Vredefort Dome experienced shock pressure > 30 GPa (Gibson  
50  
51  
52  
53  
54  
55  
56  
57  
58  
59  
60  
61  
62  
63  
64  
65

394 and Reimold 2005). The analyzed ILG zircon grains all contain {112} shock twins, a diagnostic shock  
1  
2 395 microstructure (e.g. Moser et al. 2011; Timms et al. 2012; Erickson et al. 2013a; Montalvo et al.  
3  
4 396 2017; Timms et al. in press), which have been constrained to form by 20 GPa in both shock (Leroux  
5  
6 397 et al. 1999) and static (Morozova 2015) experiments . Within partially metamict, dark CL cores in  
7  
8 398 some domains of ILG zircon grains, cross-cutting, CL bright lamellae lie along the trace of indexed  
9  
10 399 {112} twins on the polished surface. However the bright lamellae share the crystallographic  
11  
12 400 orientation of the parent grains and yield higher quality diffraction patterns compared to the CL dark  
13  
14 401 core (Fig. 3). The bright lamellae are interpreted to be {112} shock twins that annealed back to the  
15  
16 402 host zircon orientation. The core domains therefore preserve evidence of the former presence of the  
17  
18 403 shock microstructures that were annealed after the shock pulse, either by high post-shock  
19  
20 404 temperatures (cf. Gibson 2002) or subsequent tectonometamorphic activity (Moser et al. 2011).

26 405 The provenance of the shocked monazite xenocrysts within AIM is more obscure. The impact  
27  
28 406 melt is derived locally from adjacent basement granite (Silva et al. 2016) which is supported by the  
29  
30 407 similar microstructural character of all analyzed monazite grains. Shocked zircon grains from  
31  
32 408 Araguinha contain granular microstructure (cf. Bohor et al. 1993), which has been interpreted to  
33  
34 409 form at higher impact pressures, after the formation of twins or transformation to reidite (Wittmann  
35  
36 410 et al. 2006). Formation conditions of granular zircon are not experimentally calibrated and are thus  
37  
38 411 poorly constrained; metamictization of the lattice could lower the P-T requirements for the  
39  
40 412 formation of granular zircon. Systematic misorientation relationships between the neoblasts and  
41  
42 413 shocked host (Fig. 6) are consistent with granular texture formation after twinning and reidite  
43  
44 414 transformation (cf. Cavosie et al. 2016; Timms et al. 2017). Shock-generated reidite, from both  
45  
46 415 experimental and natural studies, forms a systematic inter-crystalline misorientation relationship  
47  
48 416 with the parent zircon, by which  $\langle 110 \rangle_{\text{zircon}}$  and  $\langle 110 \rangle_{\text{reidite}}$  are aligned and  $[001]_{\text{zircon}}$  is aligned with  
49  
50 417 the conjugate  $\langle 110 \rangle_{\text{reidite}}$  (Leroux et al. 1999; Reddy et al. 2015; Cavosie et al. 2015b; Erickson et al.  
51  
52 418 2017). It is therefore predicted that reversion of reidite to zircon produces domains with systematic  
53  
54 419  $90^\circ / \langle 110 \rangle$  misorientation with the original host zircon orientation (Cavosie et al. 2016; Erickson et  
55  
56  
57  
58  
59  
60  
61  
62  
63  
64  
65

1  
2 420 al. 2017; Timms et al. 2017). Thus, evidence for the former presence of reidite requires that the  
3  
4 421 rocks achieved minimum shock pressure conditions of 30 GPa, based on shock experiments (Kusaba  
5  
6 422 et al. 1985; Leroux et al. 1999). Because metamictization of zircon crystal structure inhibits the  
7  
8 423 formation of reidite (Lang et al. 2008; Erickson et al. 2017; Timms et al. in press), the systematically  
9  
10 424 misoriented granules therefore require the preexisting zircon to have been crystalline, which  
11  
12 425 supports our interpreted shock pressure.  
13

#### 14 15 426 **Shocked monazite as an impact chronometer**

16  
17 427         These results show that determining the age of a shock event from deformed monazite is  
18  
19 428 possible thorough characterization of specific microstructures that can be correlated to *in situ* U – Th  
20  
21 429 – Pb ages. All analyses from strained domains at both sites are >10% discordant between the  
22  
23 430  $^{207}\text{Pb}/^{206}\text{Pb}$  and  $^{206}\text{Pb}/^{238}\text{U}$  systems. Ages from strained domains of the ILG range from 2537 to 2386  
24  
25 431 Ma, however a regression from known age of the Vredefort impact, 2020 Ma, does not result in a  
26  
27 432 meaningful upper intercept that corresponds to a known age for the basement of the Vredefort  
28  
29 433 Dome. These results suggest that there is variable mobility of U, Th and radiogenic Pb during shock  
30  
31 434 deformation (Fig. 9 a). If correct, the implication is that shock deformation enhances the migration  
32  
33 435 of both substitutional and interstitial ions. Partial age resetting resulting from the formation and  
34  
35 436 migration of fast diffusion pathways created during the shock event may have resulted in a  
36  
37 437 significant discordia array; subsequent deformation within the Kaapvaal Craton and/or modern Pb-  
38  
39 438 loss has further modified the measured ages. Likewise, age data from shock-deformed monazite  
40  
41 439 from bedrock of the Vredefort Dome (Flowers et al. 2003), and Vredefort-sourced detrital shocked  
42  
43 440 monazite (Erickson et al. 2013b), that are dominated by lamellar microstructures, which we here  
44  
45 441 interpret to be deformation twins, record ages from ca. 3180 Ma to ca. 2157 Ma, and often do not  
46  
47 442 represent meaningful geologic ages.  
48  
49

50  
51 443         The Paleozoic age of the basement and impact event of the Araguinha structure (Tohver et  
52  
53 444 al. 2012), complicates use of the  $^{207}\text{Pb}/^{235}\text{U}$  system, however,  $^{206}\text{Pb}/^{238}\text{U}$  ages from strained domains  
54  
55 445 within Araguinha monazite range from 467 to 278 Ma. Measuring strain by EBSD from the area of  
56  
57  
58  
59  
60  
61  
62  
63  
64  
65

1  
2  
3  
4  
5  
6  
7  
8  
9  
10  
11  
12  
13  
14  
15  
16  
17  
18  
19  
20  
21  
22  
23  
24  
25  
26  
27  
28  
29  
30  
31  
32  
33  
34  
35  
36  
37  
38  
39  
40  
41  
42  
43  
44  
45  
46  
47  
48  
49  
50  
51  
52  
53  
54  
55  
56  
57  
58  
59  
60  
61  
62  
63  
64  
65

446 the SHRIMP analytical spot reveals that the three oldest ages recorded in the AIM are preserved in  
447 the least strained domains of the parent grains (Fig. 8 a). We therefore interpret the age spread  
448 within the U – Th – Pb systematics from the strained host domains to represent partial Pb-loss and  
449 mobility of U and Th as a result of fast diffusion pathways formed during the shock event. The  
450 subsequent reactivation of these hypothesized pathways by later deformation in the case of the ILG  
451 did not occur in grains from Araguainha.

452 The results of this study demonstrate that *in situ* analysis of shock-produced neoblastic  
453 monazite by SIMS can be used to date impact events. Neoblastic monazite domains from the ILG and  
454 AIM both yield concordant, young U-Pb ages, consistent with the age of the impact events  
455 constrained by independent means. The process of neoblast growth, therefore, occurs free of  
456 inherited radiogenic Pb from the parent grain. Analyses of neoblastic monazite from the ILG are less  
457 than 10 % discordant between the  $^{207}\text{Pb}/^{206}\text{Pb}$  and  $^{206}\text{Pb}/^{238}\text{U}$  systems, and the nine most concordant  
458 analyses record a weighted mean  $^{207}\text{Pb}/^{206}\text{Pb}$  age of  $2010 \pm 15$  Ma (MSWD = 0.84), within error of  
459 the 2020 Ma Vredefort impact event based on zircon from impact melt and recrystallized zircon  
460 (Kamo et al. 1996; Gibson et al. 1997; Moser 1997). The age from the neoblastic domains is also  
461 within error the most concordant ID-TIMS  $^{207}\text{Pb}/^{206}\text{Pb}$  age of granular monazite by Moser (1997),  
462  $2016 \pm 7$  Ma. The other grain analyzed by Moser (1997) is older ( $2090 \pm 4$  Ma), more discordant, and  
463 may represent a mixing age between the neoblasts and domains that retain pre-impact radiogenic  
464 Pb. This contrasts with U – Pb results from strained monazite grains, which preserve relatively  
465 discordant data with a wide age range, which do not necessarily correspond to a significant geologic  
466 date. The  $^{207}\text{Pb}/^{206}\text{Pb}$  age from the ILG neoblastic monazite is consistent with the impact event,  
467 however, analysis of the  $^{206}\text{Pb}/^{238}\text{U}$  and  $^{208}\text{Pb}/^{232}\text{Th}$  systematics reveal open system behavior and  
468 thus yield younger ages (Fig. 9). Minor discordance within neoblastic domains from the ILG monazite  
469 is likely due to subsequent tectonic events in the Kaapvaal Craton after the Vredefort impact event.  
470 Deformation after the shock event at the Vredefort Dome has likely annealed some of the shock  
471 features within zircon from the ILG (e.g. Fig. 3), and has been shown to partially reset the U – Pb

1  
2 472 isotopic system in zircon from the ILG at ca. 1100 Ma (Moser et al. 2011), the age of mafic intrusions  
3 473 within the Kaapvaal (Reimold et al. 2000). Consideration of the subsequent geologic events is  
4 474 therefore also important when interpreting the age data from complex monazite grains, as they may  
5 475 cause partial resetting due to Pb mobility. In the case of the ILG the post-shock deformation not only  
6 476 reactivated suspected fast diffusion pathways in the deformed parent domains but also caused  
7 477 minor Pb-loss within the neoblasts.

8  
9 478 Neoblasts from AIM yield a concordia age of  $259 \pm 5$  Ma (MSWD = 1.3), which is within error  
10 479 of the age of  $255 \pm 3$  Ma reported by Tohver et al. (2012). However, if only analyses from grain 11  
11 480 are considered, all of which are within uncertainty of concordia and have the lowest measured  
12 481 common Pb ( $F^{206}\text{Pb} \% >5$ ), they yield a slightly older and more precise age of  $262 \pm 3$  Ma (MSWD =  
13 482 0.88). The data from grain 10, which has been omitted, are from analytical spots on or near cracks  
14 483 and have the greatest measured common Pb and discordance between the U and Th systematics.  
15 484 Therefore, we suggest that the age of the Araguinha impact structure may be  $262 \pm 3$  Ma, which is  
16 485 slightly older than the  $255 \pm 3$  Ma determined previously, and highlight that further, careful analyses  
17 486 of neoblastic monazite domains could help to resolve the discrepancy.

18 487 Formation of neoblastic domains within monazite during shock appear to be a  
19 488 recrystallization process, whereby new monazite nucleates within the shock-deformed and strained  
20 489 lattice of the host and consumes the deformed lattice through the process of grain boundary  
21 490 migration. Similar deformation mechanisms have been identified in deformed monazite from the  
22 491 lower crust (Erickson et al. 2015), in zircon that has been tectonically-strained (Piazolo et al. 2012)  
23 492 and shock-deformed (Cavosie et al. 2015a; Timms et al. 2017) and in shocked baddeleyite (Darling et  
24 493 al. 2016). During the growth of neoblasts, incompatible ions are not incorporated into the newly  
25 494 formed lattice and thus the shock event and associated high temperature pulse sets the age of the  
26 495 neoblasts.

27 496 Results from both the ILG and AIM highlight the value in directly linking quantitative  
28 497 microstructural analyses with *in situ* geochronologic analyses in shocked monazite to directly date



1  
2 498 impact structures, which is often challenging (Jourdan et al. 2009; Jourdan et al. 2012). Results from  
3  
4 499 the Vredefort Dome also highlight the benefit of monazite, relative to other geochronometers, in  
5  
6 500 terranes which have experienced subsequent geologic complexity. This is highlighted by the fact that  
7  
8 501 although there is a ca. 1100 Ma overprint within the Vredefort Dome (Moser et al. 2011), the impact  
9  
10 502 age is recorded in neoblastic domains from the ILG monazite. Furthermore, zircon analyzed from the  
11  
12 503 ILG in this study only record crystal-plastic microstructures, which, in some cases, may be used to  
13  
14 504 determine an impact age from a discordia trend (e.g. Moser et al. 2009; Moser et al. 2011) but in  
15  
16 505 others may not (e.g. Schmieder et al. 2015; Cavosie et al. 2015a). As there is evidence of annealing of  
17  
18 506 shock features in zircon , a discordia trend between the crystallization age of the zircon and the  
19  
20 507 impact event at 2020 Ma may be obscured by subsequent Pb-loss, while the neoblastic monazite  
21  
22 508 preserve the  $^{207}\text{Pb}/^{206}\text{Pb}$  age of the impact event. Furthermore, monazite maintains a crystalline  
23  
24 509 state and is not subject to metamictization (Meldrum et al. 1998; Seydoux-Guillaume et al. 2004).  
25  
26 510 Therefore, while metamict softening of the zircon crystal lattice may inhibit the formation of shock  
27  
28 511 features such as twins or reidite (Lang et al. 2008; Erickson et al. 2017; Timms et al. in press),  
29  
30 512 monazite can unambiguously record the shock conditions, especially as a wide range of shock twins  
31  
32 513 form in monazite, possibly due to varying conditions (Erickson et al. 2016a). These results show that  
33  
34 514 monazite is subject to dynamic recrystallization at lower shock conditions than crystalline (i.e. non-  
35  
36 515 matamict) zircon, and can therefore be used to date impact structures when other geochronometers  
37  
38 516 may not record the impact age.  
39  
40  
41  
42  
43  
44

## 45 517 **Conclusions**

46  
47  
48  
49 518 This study shows that monazite grains can record both diagnostic shock features and form  
50  
51 519 neoblasts by dynamic recrystallization over a range of impact conditions. Shock microstructures  
52  
53 520 within monazite, documented herein, include deformation twins and PDBs. Deformation twins were  
54  
55 521 found as compound and/or type one twins in (001), (100),  $(10\bar{1})$ , {110}, {212}, and as type two  
56  
57 522 (irrational) twin planes with rational shear directions ( $\eta_1$ ) in  $[0\bar{1}\bar{1}]$  and  $[\bar{1}\bar{1}0]$ . In addition, during the  
58  
59  
60  
61  
62  
63  
64  
65

1 523 post-shock thermal pulse, neoblastic monazite may nucleate within the strained parent lattice and  
2 524 consume the strained lattice by grain boundary migration. Associated pressures have been  
3  
4 525 constrained by microstructural analyses of zircon from the same samples. Shock twins within the ILG  
5  
6 526 zircon record minimum impact pressures of 20 GPa, while systematically misoriented neoblasts  
7  
8  
9 527 within Araguinha zircon require minimum pressures of 30 GPa or higher.

10  
11  
12 528 *In situ* U – Th – Pb SIMS analyses of strained domains record discordant age arrays which may  
13  
14 529 allow resolution of impact age, depending on subsequent geologic history of the structure. Analysis  
15  
16 530 of monazite neoblasts from the ILG by SIMS yield a  $^{207}\text{Pb}/^{206}\text{Pb}$  age of  $2010 \pm 15$  Ma, consistent with  
17  
18  
19 531 the accepted 2020 Ma age of the Vredefort impact. Likewise, analysis of monazite neoblasts from  
20  
21 532 the AIM yield a concordia age of  $259 \pm 5$  Ma, which we interpret as the date of the Araguinha  
22  
23 533 shock event. Because impact events are challenging to date (Jourdan et al. 2009), these results  
24  
25  
26 534 represent a significant advance in resolving impact ages. For example, of the 27 Precambrian impact  
27  
28 535 structures (Spray and Hines 2016), only 4 have precise ages (Jourdan et al. 2009). This study shows  
29  
30  
31 536 that coupling EBSD analyses of monazite microstructures with targeted high resolution U – Th – Pb  
32  
33 537 analyses either by SIMS or LA-ICPMS, offers another method for which to date impact structures,  
34  
35 538 including Precambrian (e.g. Vredefort) and Phanerozoic (e.g. Araguinha) impact structures, even  
36  
37  
38 539 those that have experienced subsequently tectonic deformation.

## 41 540 **Acknowledgments**

42  
43  
44 541 TME acknowledges financial support from an International Post-Graduate Research Grant  
45  
46 542 from Curtin University Office of Research and Development and from the ARC Core to Crust Fluid  
47  
48  
49 543 System COE. The ARC (LE130100053), Curtin University, University of Western Australia and CSIRO  
50  
51 544 are acknowledged for funding the Tescan Mira3 FEG-SEM housed in the John De Laeter  
52  
53 545 Centre's Microscopy & Microanalysis Facility. The authors would like to thank Ben Wade at Adelaide  
54  
55  
56 546 Microscopy for collecting the EPMA maps. We would like to thank two anonymous reviewers and  
57  
58  
59  
60  
61  
62  
63  
64  
65

547 editor Prof. O. Müntener for the detailed and insightful comments that have substantially improved  
1  
2 548 this manuscript.  
3

## 549 Citations

- 550 Armstrong RA, Lana C, Uwe Reimold W, Gibson RL (2006) SHRIMP zircon age constraints on  
551 Mesoarchean crustal development in the Vredefort dome, central Kaapvaal Craton, South  
552 Africa Geological Society of America Special Papers 405:233-253 doi:10.1130/2006.2405(13)  
553 Bischoff AA, Mayer JJ, Voors WA, Retief PF (1999) Geology of the Vredefort Dome. Council for  
554 Geoscience, Pretoria  
555 Bohor BF, Betterton WJ, Krogh TE (1993) Impact-shocked zircons: discovery of shock-induced  
556 textures reflecting increasing degrees of shock metamorphism Earth and Planetary Science  
557 Letters 119:419-424 doi:[http://dx.doi.org/10.1016/0012-821X\(93\)90149-4](http://dx.doi.org/10.1016/0012-821X(93)90149-4)  
558 Buick IS, Clark C, Rubatto D, Hermann J, Pandit M, Hand M (2010) Constraints on the Proterozoic  
559 evolution of the Aravalli–Delhi Orogenic belt (NW India) from monazite geochronology and  
560 mineral trace element geochemistry Lithos 120:511-528 doi:10.1016/j.lithos.2010.09.011  
561 Catlos EJ (2013) Versatile Monazite: resolving geological records and solving challenges in materials  
562 science: Generalizations about monazite: Implications for geochronologic studies American  
563 Mineralogist 98:819-832 doi:10.2138/am.2013.4336  
564 Cavosie AJ, Erickson TM, Montalvo P, Prado D, Cintron N, Gibbon RJ (in press) The Rietputs  
565 Formation in South Africa: A Pleistocene fluvial archive of meteorite impact unique to the  
566 Kaapvaal craton. In: Moser DE, Corfu F, Reddy SM, Darling J, Tait K (eds) Microstructural  
567 Geochronology; Lattice to Atom-Scale Records of Planetary Evolution. AGU Monograph.  
568 AGU-Wiley,  
569 Cavosie AJ, Erickson TM, Timms NE (2015b) Nanoscale records of ancient shock deformation: Reidite  
570 (ZrSiO<sub>4</sub>) in sandstone at the Ordovician Rock Elm impact crater Geology 43:315-318  
571 doi:10.1130/g36489.1  
572 Cavosie AJ, Erickson TM, Timms NE, Reddy SM, Talavera C, Montalvo SD, Pincus MR, Gibbon RJ,  
573 Moser D (2015a) A terrestrial perspective on using ex situ shocked zircons to date lunar  
574 impacts Geology 43:999-1002 doi:10.1130/g37059.1  
575 Cavosie AJ, Quintero RR, Radovan HA, Moser DE (2010) A record of ancient cataclysm in modern  
576 sand: Shock microstructures in detrital minerals from the Vaal River, Vredefort Dome, South  
577 Africa Geological Society of America Bulletin 122:1968-1980 doi:10.1130/b30187.1  
578 Cavosie AJ, Timms NE, Erickson TM, Hagerty JJ, Hörz F (2016) Transformations to granular zircon  
579 revealed: Twinning, reidite, and ZrO<sub>2</sub> in shocked zircon from Meteor Crater (Arizona, USA)  
580 Geology doi:10.1130/g38043.1  
581 D'Abzac F-X, Seydoux-Guillaume A-M, Chmeleff J, Datas L, Poitrasson F (2012) In situ characterization  
582 of infrared femtosecond laser ablation in geological samples. Part A: the laser induced  
583 damage Journal of Analytical Atomic Spectrometry 27:99-107 doi:10.1039/C1JA10153F  
584 Darling JR, Moser DE, Barker IR, Tait KT, Chamberlain KR, Schmitt AK, Hyde BC (2016) Variable  
585 microstructural response of baddeleyite to shock metamorphism in young basaltic  
586 shergottite NWA 5298 and improved U–Pb dating of Solar System events Earth and  
587 Planetary Science Letters 444:1-12 doi:<http://dx.doi.org/10.1016/j.epsl.2016.03.032>  
588 Deutsch A, Schärer U (1990) Isotope systematics and shock-wave metamorphism: I. U-Pb in zircon,  
589 titanite and monazite, shocked experimentally up to 59 GPa Geochimica et Cosmochimica  
590 Acta 54:3427-3434 doi:[http://dx.doi.org/10.1016/0016-7037\(90\)90295-V](http://dx.doi.org/10.1016/0016-7037(90)90295-V)  
591 Engelhardt WV, Matthäi SK, Walzebeck J (1992) Araguinha impact crater, Brazil. I. The interior part  
592 of the uplift Meteoritics 27:442-457  
593 Erickson TM, Cavosie AJ, Moser DE, Barker IR, Radovan HA (2013a) Correlating planar  
594 microstructures in shocked zircon from the Vredefort Dome at multiple scales:

595 Crystallographic modeling, external and internal imaging, and EBSD structural analysis  
 1 596 American Mineralogist 98:53-65 doi:10.2138/am.2013.4165  
 2 597 Erickson TM, Cavosie AJ, Moser DE, Barker IR, Radovan HA, Wooden J (2013b) Identification and  
 3 598 provenance determination of distally transported, Vredefort-derived shocked minerals in  
 4 599 the Vaal River, South Africa using SEM and SHRIMP-RG techniques *Geochimica et*  
 5 600 *Cosmochimica Acta* 107:170-188 doi:<http://dx.doi.org/10.1016/j.gca.2012.12.008>  
 7 601 Erickson TM, Cavosie AJ, Pearce MA, Timms NE, Reddy SM (2016a) Empirical constraints on shock  
 8 602 features in monazite using shocked zircon inclusions *Geology* 44:635-638  
 9 603 doi:10.1130/g37979.1  
 10 604 Erickson TM, Pearce MA, Reddy SM, Timms NE, Cavosie AJ, Bourdet J, Rickard WDA, Nemchin AA  
 11 605 (2017) Microstructural constraints on the mechanisms of the transformation to reidite in  
 12 606 naturally shocked zircon *Contributions to Mineralogy and Petrology* doi:10.1007/s00410-  
 14 607 016-1322-0  
 15 608 Erickson TM, Pearce MA, Taylor RJM, Timms NE, Clark C, Reddy SM, Buick IS (2015) Deformed  
 16 609 monazite yields high-temperature tectonic ages *Geology* 43:383-386 doi:10.1130/g36533.1  
 17 610 Erickson TM, Reddy SM, Timms NE, Pearce MA, Taylor RJM, Clark C, Buick IS (2016b) Deformed  
 18 611 monazite yields high-temperature tectonic ages: REPLY *Geology* 44:e378-e378  
 20 612 doi:10.1130/g37474y.1  
 21 613 Fletcher IR, McNaughton NJ, Davis WJ, Rasmussen B (2010) Matrix effects and calibration limitations  
 22 614 in ion probe U–Pb and Th–Pb dating of monazite *Chemical Geology* 270:31-44  
 23 615 doi:10.1016/j.chemgeo.2009.11.003  
 24 616 Flowers RM, Moser DE, Hart R (2003) Evolution of the Amphibolite-Granulite Facies Transition  
 25 617 Exposed by the Vredefort Impact Structure, Kaapvaal Craton, South Africa *The Journal of*  
 26 618 *Geology* 111:455-470 doi:10.1086/375282  
 28 619 French BM, Koeberl C (2010) The convincing identification of terrestrial meteorite impact structures:  
 29 620 What works, what doesn't, and why *Earth-Science Reviews* 98:123-170  
 30 621 doi:10.1016/j.earscirev.2009.10.009  
 31 622 Gibson RL (2002) Impact-induced melting of Archean granulites in the Vredefort Dome, South Africa.  
 32 623 I: anatexis of metapelitic granulites *Journal of Metamorphic Geology* 20:57-70  
 34 624 doi:10.1046/j.0263-4929.2001.00358.x  
 35 625 Gibson RL, Armstrong RA, Reimold WU (1997) The age and thermal evolution of the Vredefort  
 36 626 impact structure: A single-grain U • Pb zircon study *Geochimica et Cosmochimica Acta*  
 37 627 61:1531-1540 doi:[http://dx.doi.org/10.1016/S0016-7037\(97\)00013-6](http://dx.doi.org/10.1016/S0016-7037(97)00013-6)  
 39 628 Gibson RL, Reimold WU (2005) Shock pressure distribution in the Vredefort impact structure, South  
 40 629 Africa *Geological Society of America Special Papers* 384:329-349 doi:10.1130/0-8137-2384-  
 41 630 1.329  
 42 631 Gibson RL, Uwe Reimold W, Stevens G (1998) Thermal-metamorphic signature of an impact event in  
 43 632 the Vredefort dome, South Africa *Geology* 26:787-790 doi:10.1130/0091-  
 44 633 7613(1998)026<0787:tmsoai>2.3.co;2  
 45 634 Grieve RA, Dence M, Robertson P Cratering processes-As interpreted from the occurrence of impact  
 46 635 melts. In: *Impact and explosion cratering: Planetary and terrestrial implications, 1977.* pp  
 47 636 791-814  
 49 637 Hart R, Moser D, Andreoli M (1999) Archean age for the granulite facies metamorphism near the  
 50 638 center of the Vredefort structure, South Africa *Geology* 27:1091-1094 doi:10.1130/0091-  
 51 639 7613(1999)027<1091:aaftgf>2.3.co;2  
 52 640 Hay RS, Marshall DB (2003) Deformation twinning in monazite *Acta Materialia* 51:5235-5254  
 53 641 doi:10.1016/s1359-6454(03)00305-7  
 54 642 Ivanov BA (2005) Numerical Modeling of the Largest Terrestrial Meteorite Craters *Solar System*  
 55 643 *Research* 39:381-409  
 56 644 Jourdan F, Reimold WU, Deutsch A (2012) Dating Terrestrial Impact Structures *Elements* 8:49-53  
 57 645 doi:10.2113/gselements.8.1.49

- 646 Jourdan F, Renne PR, Reimold WU (2009) An appraisal of the ages of terrestrial impact structures  
1 647 Earth and Planetary Science Letters 286:1-13 doi:10.1016/j.epsl.2009.07.009
- 2 648 Kamo SL, Reimold WU, Krogh TE, Colliston WP (1996) A 2.023 Ga age for the Vredefort impact event  
3 649 and a first report of shock metamorphosed zircons in pseudotachylitic breccias and  
4 650 Granophyre Earth and Planetary Science Letters 144:369-387  
5 651 doi:[http://dx.doi.org/10.1016/S0012-821X\(96\)00180-X](http://dx.doi.org/10.1016/S0012-821X(96)00180-X)
- 7 652 Kusaba K, Syono Y, Kikuchi M, Fukuoka K (1985) Shock behavior of zircon: phase transition to  
8 653 scheelite structure and decomposition Earth and Planetary Science Letters 72:433-439  
9 654 doi:[http://dx.doi.org/10.1016/0012-821X\(85\)90064-0](http://dx.doi.org/10.1016/0012-821X(85)90064-0)
- 11 655 Lana C, Filho CRS, Marangoni YR, Yokoyama E, Trindade RIF, Tohver E, Reimold WU (2007) Insights  
12 656 into the morphology, geometry, and post-impact erosion of the Araguinha peak-ring  
13 657 structure, central Brazil Geological Society of America Bulletin 119:1135-1150  
14 658 doi:10.1130/b26142.1
- 16 659 Lana C, Filho CRS, Marangoni YR, Yokoyama E, Trindade RIF, Tohver E, Reimold WU (2008) Structural  
17 660 evolution of the 40 km wide Araguinha impact structure, central Brazil Meteoritics &  
18 661 Planetary Science 43:701-716 doi:10.1111/j.1945-5100.2008.tb00679.x
- 19 662 Lang M, Zhang F, Lian J, Trautmann C, Neumann R, Ewing RC (2008) Irradiation-induced stabilization  
20 663 of zircon (ZrSiO<sub>4</sub>) at high pressure Earth and Planetary Science Letters 269:291-295  
21 664 doi:10.1016/j.epsl.2008.02.027
- 22 665 Langenhorst F, Deutsch A (2012) Shock Metamorphism of Minerals Elements 8:31-36  
23 666 doi:10.2113/gselements.8.1.31
- 25 667 Leroux H, Reimold WU, Koeberl C, Hornemann U, Doukhan JC (1999) Experimental shock  
26 668 deformation in zircon: a transmission electron microscopic study Earth and Planetary  
27 669 Science Letters 169:291-301 doi:[http://dx.doi.org/10.1016/S0012-821X\(99\)00082-5](http://dx.doi.org/10.1016/S0012-821X(99)00082-5)
- 28 670 Machado R, Lana C, Stevens G, Filho CRS, Reimold WU, McDonald I (2009) Generation, mobilization  
29 671 and crystallization of impact-induced alkali-rich melts in granitic target rocks: Evidence from  
30 672 the Araguinha impact structure, central Brazil Geochimica et Cosmochimica Acta 73:7183-  
31 673 7201 doi:<http://dx.doi.org/10.1016/j.gca.2009.08.029>
- 33 674 Meldrum A, Boatner LA, Weber WJ, Ewing RC (1998) Radiation damage in zircon and monazite  
34 675 Geochimica et Cosmochimica Acta 62:2509-2520 doi:[http://dx.doi.org/10.1016/S0016-7037\(98\)00174-4](http://dx.doi.org/10.1016/S0016-7037(98)00174-4)
- 36 676
- 37 677 Melosh J (1989) Impact Cratering: A geologic process.
- 38 678 Montalvo SD, Cavosie AJ, Erickson TM, Talavera C (2017) Fluvial transport of impact evidence from  
39 679 cratonic interior to passive margin: Vredefort-derived shocked zircon on the Atlantic coast of  
40 680 South Africa American Mineralogist in press doi:10.2138/am-2017-5857CCBYNCND
- 41 681 Morozova I (2015) Strength Study of Zircon Under High Pressure. The University of Western Ontario
- 42 682 Moser DE (1997) Dating the shock wave and thermal imprint of the giant Vredefort impact, South  
43 683 Africa Geology 25:7-10 doi:10.1130/0091-7613(1997)025<0007:dtswat>2.3.co;2
- 45 684 Moser DE, Cupelli CL, Barker IR, Flowers RM, Bowman JR, Wooden J, Hart JR (2011) New zircon shock  
46 685 phenomena and their use for dating and reconstruction of large impact structures revealed  
47 686 by electron nanobeam (EBSD, CL, EDS) and isotopic U–Pb and (U–Th)/He analysis of the  
48 687 Vredefort dome Canadian Journal of Earth Sciences 48:117-139 doi:10.1139/e11-011
- 49 688 Moser DE, Davis WJ, Reddy SM, Flemming RL, Hart RJ (2009) Zircon U–Pb strain chronometry reveals  
50 689 deep impact-triggered flow Earth and Planetary Science Letters 277:73-79  
51 690 doi:10.1016/j.epsl.2008.09.036
- 53 691 Moser DE, Flowers RM, Hart RJ (2001) Birth of the Kaapvaal tectosphere 3.08 billion years ago  
54 692 Science 291:465-468 doi:10.1126/science.291.5503.465
- 55 693 Niihara T, Kaiden H, Misawa K, Sekine T, Mikouchi T (2012) U–Pb isotopic systematics of shock-  
56 694 loaded and annealed baddeleyite: Implications for crystallization ages of Martian meteorite  
57 695 shergottites Earth and Planetary Science Letters 341–344:195-210  
58 696 doi:<http://dx.doi.org/10.1016/j.epsl.2012.06.002>
- 59 696

- 697 Piazolo S, Austrheim H, Whitehouse M (2012) Brittle-ductile microfabrics in naturally deformed  
1 698 zircon: Deformation mechanisms and consequences for U-Pb dating *American Mineralogist*  
2 699 97:1544-1563 doi:10.2138/am.2012.3966
- 3 700 Reddy SM, Johnson TE, Fischer S, Rickard W, Taylor RJM (2015) Precambrian redite discovered in  
4 701 shocked zircon from the Stac Fada impactite, Scotland *Geology* Accepted
- 5 702 Reddy SM, Timms NE, Pantleon W, Trimby P (2007) Quantitative characterization of plastic  
6 703 deformation of zircon and geological implications *Contributions to Mineralogy and Petrology*  
7 704 153:625-645 doi:10.1007/s00410-006-0174-4
- 8 705 Reimold WU, Pybus GQJ, Kruger FJ, Layer PW, Koeberl C (2000) The Anna's Rust Sheet and related  
9 706 gabbroic intrusions in the Vredefort Dome-Kibaran magmatic event on the Kaapvaal Craton  
10 707 and beyond? *Journal of African Earth Sciences* 31:499-521  
11 708 doi:[http://dx.doi.org/10.1016/S0899-5362\(00\)80004-4](http://dx.doi.org/10.1016/S0899-5362(00)80004-4)
- 12 709 Schärer U, Deutsch A (1990) Isotope systematics and shock-wave metamorphism: II. U-Pb and Rb-Sr  
13 710 in naturally shocked rocks; the Houghton Impact Structure, Canada *Geochimica et*  
14 711 *Cosmochimica Acta* 54:3435-3447 doi:[http://dx.doi.org/10.1016/0016-7037\(90\)90296-W](http://dx.doi.org/10.1016/0016-7037(90)90296-W)
- 15 712 Schmieder M, Tohver E, Jourdan F, Denyszyn SW, Haines PW (2015) Zircons from the Acraman  
16 713 impact melt rock (South Australia): Shock metamorphism, U-Pb and <sup>40</sup>Ar/<sup>39</sup>Ar systematics,  
17 714 and implications for the isotopic dating of impact events *Geochimica et Cosmochimica Acta*  
18 715 161:71-100 doi:<http://dx.doi.org/10.1016/j.gca.2015.04.021>
- 19 716 Seydoux-Guillaume A-M, Freydier R, Poitrasson F, D'Abzac F-x, Wirth R, Datas L (2010) Dominance of  
20 717 mechanical over thermally induced damage during femtosecond laser ablation of monazite  
21 718 *European Journal of Mineralogy* 22:235-244 doi:10.1127/0935-1221/2010/0022-2001
- 22 719 Seydoux-Guillaume A-M, Wirth R, Deutsch A, Schärer U (2004) Microstructure of 24-1928 Ma  
23 720 concordant monazites; implications for geochronology and nuclear waste deposits  
24 721 *Geochimica et Cosmochimica Acta* 68:2517-2527  
25 722 doi:<http://dx.doi.org/10.1016/j.gca.2003.10.042>
- 26 723 Silva D, Lana C, de Souza Filho CR (2016) Petrographic and geochemical characterization of the  
27 724 granitic rocks of the Araguinha impact crater, Brazil *Meteoritics & Planetary Science*  
28 725 51:443-467 doi:10.1111/maps.12601
- 29 726 Spray J, Hines J (2016) Earth Impact Database. Planetary and Space Science Centre, University of  
30 727 New Brunswick. <http://www.passc.net/EarthImpactDatabase/>. 2016
- 31 728 Stepto D (1990) The geology and gravity field in the central core of the Vredefort structure  
32 729 *Tectonophysics* 171:75-103 doi:[http://dx.doi.org/10.1016/0040-1951\(90\)90091-L](http://dx.doi.org/10.1016/0040-1951(90)90091-L)
- 33 730 Stöffler D, Langenhorst F (1994) Shock metamorphism of quartz in nature and experiment: I. Basic  
34 731 observation and theory\* *Meteoritics* 29:155-181 doi:10.1111/j.1945-5100.1994.tb00670.x
- 35 732 Timms NE, Erickson TM, Pearce MA, Cavosie AJ, Schmieder M, Tohver E, Reddy SM, Zanetti MR,  
36 733 Nemchin AA, Wittmann A (2017) A pressure-temperature phase diagram for zircon at  
37 734 extreme conditions *Earth-Science Reviews* 165:185-202  
38 735 doi:<http://dx.doi.org/10.1016/j.earscirev.2016.12.008>
- 39 736 Timms NE, Healy D, Erickson TM, Nemchin AA, Pearce MA, Cavosie AJ (in press) Role of elastic  
40 737 anisotropy in the development of deformation microstructures in zircon. In: Moser DE, Corfu  
41 738 F, Reddy SM, Darling J, Tait K (eds) *Microstructural Geochronology; Lattice to Atom-Scale*  
42 739 *Records of Planetary Evolution*. AGU Monograph. AGU-Wiley,
- 43 740 Timms NE, Reddy SM, Healy D, Nemchin AA, Grange ML, Pidgeon RT, Hart R (2012) Resolution of  
44 741 impact-related microstructures in lunar zircon: A shock-deformation mechanism map  
45 742 *Meteoritics & Planetary Science* 47:120-141 doi:10.1111/j.1945-5100.2011.01316.x
- 46 743 Tohver E, Lana C, Cawood PA, Fletcher IR, Jourdan F, Sherlock S, Rasmussen B, Trindade RIF,  
47 744 Yokoyama E, Souza Filho CR, Marangoni Y (2012) Geochronological constraints on the age of  
48 745 a Permo-Triassic impact event: U-Pb and <sup>40</sup>Ar/<sup>39</sup>Ar results for the 40km Araguinha  
49 746 structure of central Brazil *Geochimica et Cosmochimica Acta* 86:214-227  
50 747 doi:10.1016/j.gca.2012.03.005

748 Wawrzenitz N, Krohe A, Rhede D, Romer RL (2012) Dating rock deformation with monazite: The  
1 749 impact of dissolution precipitation creep *Lithos* 134-135:52-74  
2 750 doi:10.1016/j.lithos.2011.11.025  
3 751 Wittmann A, Kenkmann T, Schmitt RT, Stöffler D (2006) Shock-metamorphosed zircon in terrestrial  
4 752 impact craters *Meteoritics & Planetary Science* 41:433-454 doi:10.1111/j.1945-  
5 753 5100.2006.tb00472.x  
6  
7  
8 754  
9

## 10 755 **Figure Captions**

11  
12  
13 756 **Figure 1** Bedrock maps of the Vredefort Dome and Araguinha impact structures with sample  
14  
15 757 locations. A. Simplified bedrock map of the Vredefort Dome impact structure, South Africa, modified  
16  
17 758 from Bischoff et al. (1999). The location of sample 09SA06 (this study) is the same as V58 (Moser  
18  
19 759 1997), shocked monazite samples G2 (Hart et al. 1999) and V55 (Flowers et al. 2003) are also  
20  
21 760 marked. Shock pressure isobars are taken from Gibson and Reimold (2005). B. Simplified bedrock  
22  
23 761 map of the Araguinha impact structure, Brazil, modified from (Lana et al. 2007) with the location of  
24  
25 762 sample ARA (this study), impact melt collected from within the central uplift.

26  
27  
28  
29 763 **Figure 2** Shock deformed monazite from sample 09SA06 from the Inlandsee leucogranofels (ILG). A.  
30  
31 764 Back scatter electron (BSE) atomic number contrast photomicrographs with the location of each  
32  
33 765 SIMS U – Th – Pb analytical spot is marked on the grains. B. Electron backscatter diffraction (EBSD)  
34  
35 766 crystallographic orientation map, colored with an all Euler scheme, SIMS  $^{207}\text{Pb}/^{206}\text{Pb}$  age  
36  
37 767 measurements are marked for each spot. apatite inclusions are marked A. C. EBSD grain  
38  
39 768 misorientation map, which helps visualize the substructure of the grains by plotting the  
40  
41 769 disorientation angle of each pixel from the mean grain orientation, each SIMS spot is labeled with  
42  
43 770 the calculated average grain orientation spread (GOS avg.) for each subdomain, see text for details  
44  
45 771 of the calculation, grain boundaries are defined by disorientation threshold of  $>10^\circ$ . Blue domains  
46  
47 772 are low strains, while warm colors represent higher degrees of misorientation. Additionally,  
48  
49 773 boundaries between adjacent pixels are color coded if they matched a specific misorientation axis  
50  
51 774 and angle pair, within  $5^\circ$ , such as a known twin misorientation, . D. Electron microprobe analyzer  
52  
53 775 (EPMA) maps of Th  $\text{M}\alpha$  intensity, with measured Th concentrations (in PPM) for each SIMS spot. E.  
54  
55  
56  
57  
58  
59  
60  
61  
62  
63  
64  
65



1 776 Pole figures of monazite (010) colored with an all Euler scheme. Grain 3 is a shocked monazite which  
2 777 has completely converted to neoblasts by dynamic recrystallization. Monazite grain 7 which contains  
3  
4 778 both domains dominated by plastic strain and deformation twins and domains with low strain  
5  
6  
7 779 neoblasts. Grain 8 contains both domains dominated by plastic strain and deformation twins and  
8  
9 780 domains with low strain neoblasts.

10  
11 781 **Figure 3** Typical shocked zircon from ILG sample 09SA06. A. Cathodoluminesce (CL) image of shocked  
12  
13 782 zircon exhibiting a dark concentrically zoned core, with a brighter sector zoned rim. B. EBSD  
14  
15 783 orientation map of the zircon with an inverse pole figure (IPF<sub>2</sub>) color scheme and a special boundary  
16  
17 784 (65°/⟨110⟩) color for {112} shock twins. IPF colors correspond to crystallographic direction parallel  
18  
19 785 to the normal to the map acquisition surface (z). C. IPF and special boundary map of an area of  
20  
21 786 interest of the zircon, the {112} lamellae cross-cutting the CL-dark core have annealed to the  
22  
23 787 orientation of the host grain and correspond to bright CL lamellae. E. Pole figure of data from map B,  
24  
25 788 also with an IPF color scheme, highlighting the ⟨110⟩ misorientation axis of the shock twins.

26  
27  
28  
29  
30 789 **Figure 4** Shock deformed monazite from sample ARA from the Araguinha melt rock. A. BSE atomic  
31  
32 790 number contrasts images of the shocked monazite grains, the location of each SIMS U – Th – Pb  
33  
34 791 analytical spot is marked on grains 10 and 11. B. EBSD crystallographic orientation map, colored with  
35  
36 792 an all Euler scheme, SIMS <sup>207</sup>Pb/<sup>206</sup>Pb age measurements are marked for each spot. C. EBSD grain  
37  
38 793 misorientation map, which helps visualize the substructure of the grains by plotting each deviation  
39  
40 794 angle of each pixel from the mean grain orientation, grain boundaries are defined as >10°. Blue  
41  
42 795 domains are low strains, while warm colors represent higher degrees of misorientation, each SIMS  
43  
44 796 spot is labeled with the calculated grain orientation spread (GOS) for the area of each analytical  
45  
46 797 spot, see text for details of the calculation, uncalculated (uncalc.) values are from spots which  
47  
48 798 crossed high-angle grain boundaries. Boundaries between adjacent pixels are also color coded if  
49  
50 799 they matched a specific misorientation axis and angle pair, within 5°, such as a known twin  
51  
52 800 misorientation, a shocked zircon inclusion within grain 6 is colored with an IPF<sub>2</sub> scheme. D. EPMA Th  
53  
54 801 Mα intensity maps, with measured Th concentrations (in PPM) for each SIMS spot. E. Pole figures of  
55  
56  
57  
58  
59  
60  
61  
62  
63  
64  
65



1  
2  
3  
4  
5  
6  
7  
8  
9  
10  
11  
12  
13  
14  
15  
16  
17  
18  
19  
20  
21  
22  
23  
24  
25  
26  
27  
28  
29  
30  
31  
32  
33  
34  
35  
36  
37  
38  
39  
40  
41  
42  
43  
44  
45  
46  
47  
48  
49  
50  
51  
52  
53  
54  
55  
56  
57  
58  
59  
60  
61  
62  
63  
64  
65

802 monazite (010) colored with an all Euler scheme. Shock deformed monazite grain (10) exhibits a  
803 combination of strained parent domains, including a high concentration of planar deformation bands  
804 (PDBs), and strain free neoblasts. Monazite grain (11) in which the inner core of the grain has  
805 recrystallized to strain free neoblasts and the other domains of the grain preserve PDBs and shock  
806 twins. Shock deformed monazite (grain 6), which preserves PDBs, deformation twins, and a shocked  
807 zircon inclusion.

808 **Figure 5** High resolution EBSD maps of regions of interest from shock deformed monazite from  
809 sample ARA. BSE atomic number contrast images of each area of interest, with a inlaid CL image of  
810 the zircon inclusion from grain 6. EBSD crystallographic orientation maps colored with an all Euler  
811 scheme. EBSD grain misorientation maps, which help visualize the substructure of the grains by  
812 plotting the deviation angle of each pixel from the mean grain orientation, grain boundaries are  
813 defined as  $>10^\circ$ . Blue domains are low strains, while warm colors represent higher degrees of  
814 misorientation. The boundaries between adjacent pixels are color coded if they matched a specific  
815 misorientation axis and angle pair, within  $5^\circ$ , such as a known twin misorientation, a shocked zircon  
816 inclusion is colored with an  $IPF_z$  scheme. A. Shock deformed grain (10), with high strain domains  
817 which are remnants of the host grain and low strain neoblasts, many of which are found in  
818 orientations close to known deformation twins. Curved arrows point to some of the melt bearing  
819 sub-planar fractures within the monazite. B. Region of interest from grain 11, showing both shock  
820 twins, high strain PDBs and strain-free neoblasts. C. A region of interest from grain 6, which contains  
821 a shocked zircon inclusion. Along the edge of the zircon two domains (light-blue to purple in  $IPF_z$ )  
822 which contain plastic strain, are remnants of the parent grain, while 4 domains (dark blue, royal  
823 blue, yellow and green in  $IPF_z$ ), which are unstrained, and non-systematically misoriented from one  
824 another, are neoblastic. Note the pole figure inlay for the orientation relationships of the zircon  
825 inclusion.

826 **Figure 6** A shock deformed zircon which contains granular sub-domains. A. CL image of the shocked  
827 zircon. B. Orientation ( $IPF_z$ ) and special boundary whole grain map of the shocked zircon, the

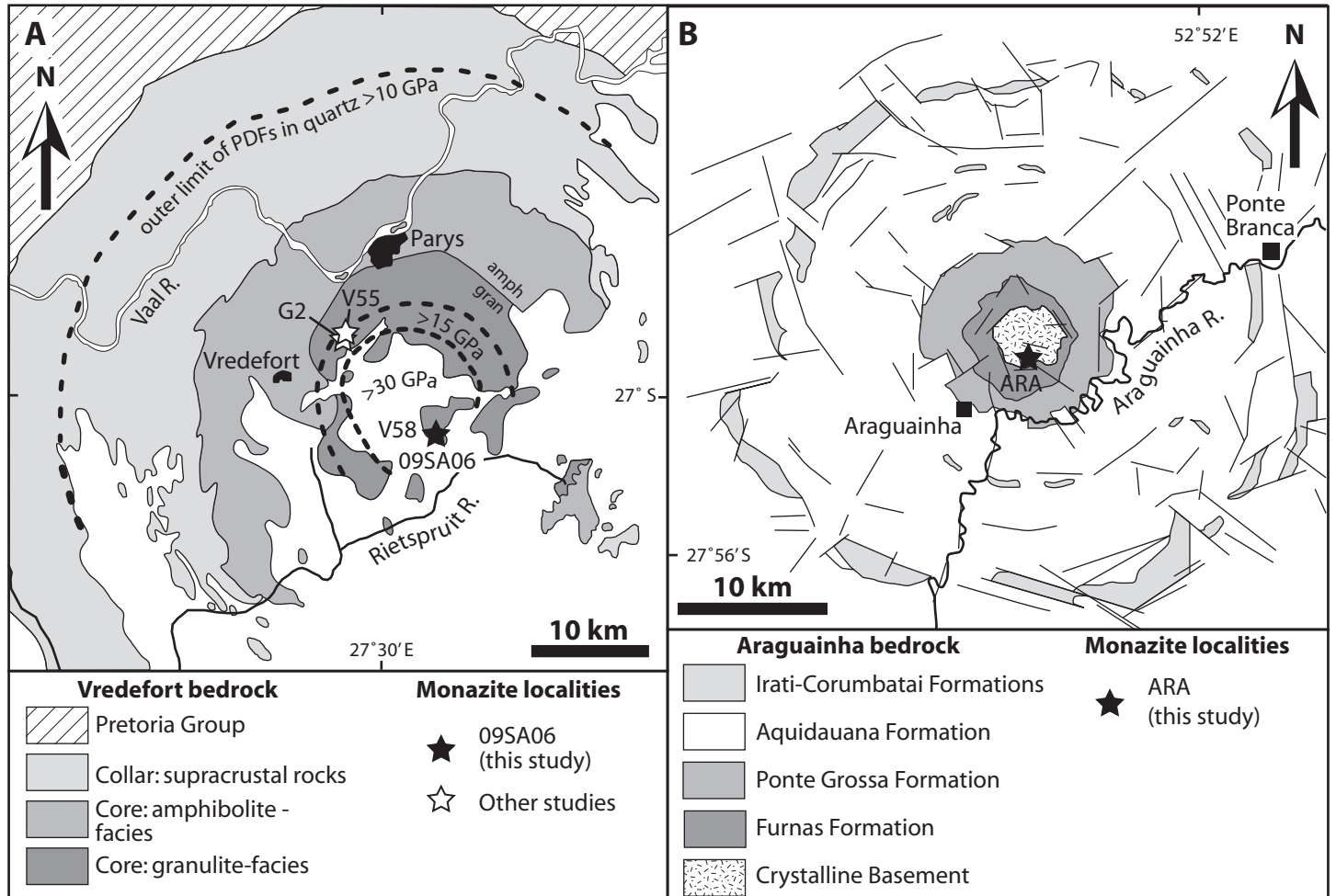
1 828 plastically strained parent orientation is colored yellow to green. C, D. High resolution region of  
2 829 interest maps of domains with a high abundance of shocked zircons. Note that many of the granules  
3  
4 830 are have systematic grain boundaries of either  $65^\circ/\langle 110 \rangle$  or  $90^\circ/\langle 110 \rangle$ , which are consistent with  
5  
6  
7 831 granules which have formed from either shock  $\{112\}$  zircon twins or the reversion of high pressure  
8  
9 832  $\text{ZrSiO}_4$  polymorph reidite, respectively (Cavosie et al. 2016). E. Pole figures of (001) and  $\{110\}$ ,  
10  
11 833 showing the systematic misorientation of the neoblastic domains, consistent with formation from  
12  
13 834 either zircon shock twins or reversion from reidite.

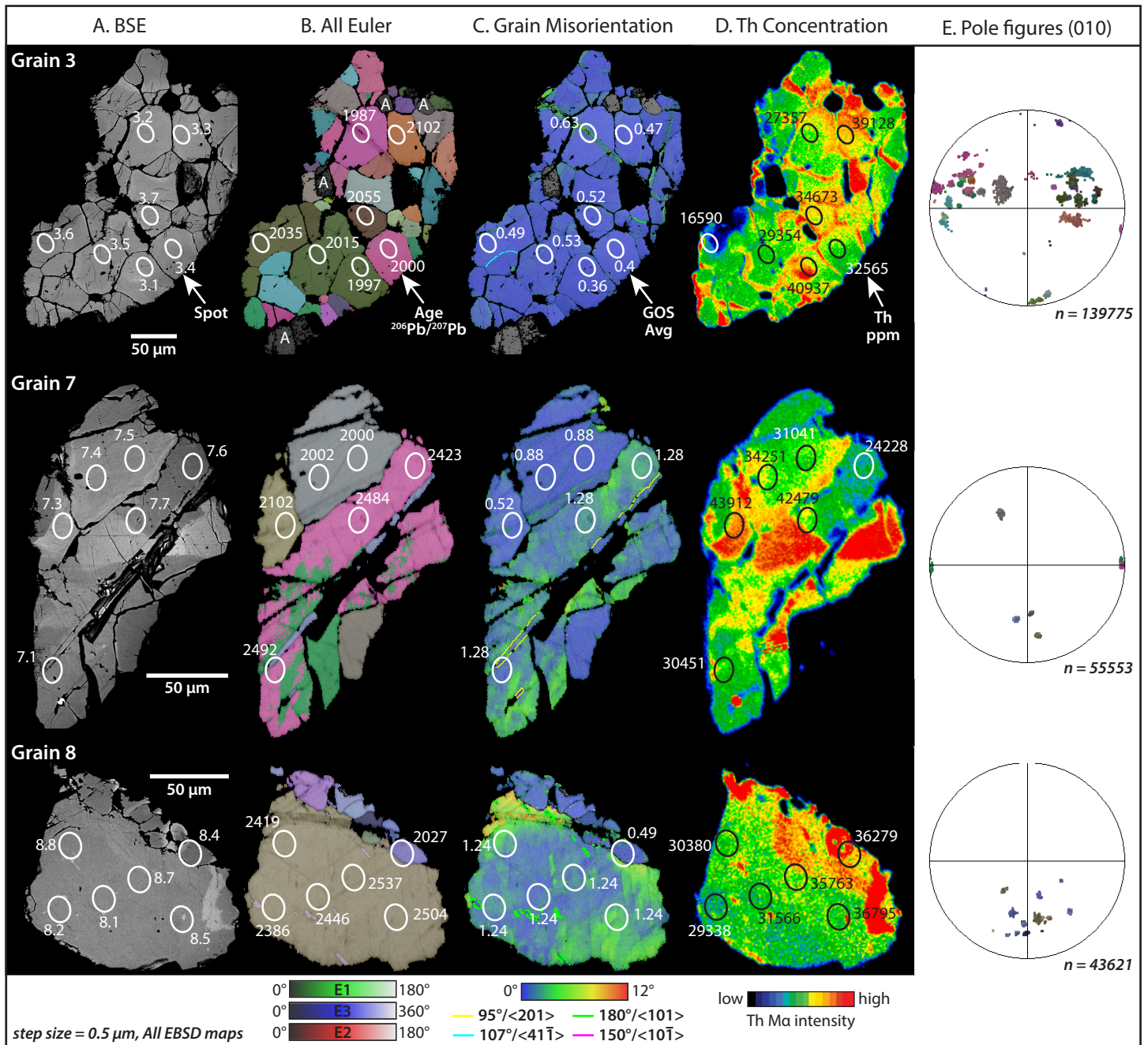
14  
15  
16 835 **Figure 7** U –Pb data for shocked monazite from sample 09SA06 from the ILG. A. Tera-Wasserburg  
17  
18 836 concordia diagram of all analyses, the spots are color-coded to average misorientation (as average  
19  
20 837 grain orientation spread) calculated within the analyzed subgrain of each spot from the EBSD data  
21  
22 838 (see appendix 1 for method). B. Tera-Wasserburg concordia diagram of neoblastic domains, color  
23  
24  
25 839 coded for discordance of the U – Th – Pb systematics. The analyses show a relative trend of  
26  
27 840 discordance with increased common Pb. All error ellipses are  $2\sigma$ .

28  
29  
30  
31 841 **Figure 8** U –Pb data for shocked monazite from sample ARA from the Araguinha melt rocks. A. Tera-  
32  
33 842 Wasserburg concordia diagram of all analyses, the spots are color-coded to misorientation (as grain  
34  
35 843 orientation spread) calculated within the analytical area of each spot from the EBSD data, purple  
36  
37 844 analyses were uncalculated (uncalc.) because the spot crossed a grain boundary (see appendix 1 for  
38  
39 845 method). B. Tera-Wasserburg concordia diagram for neoblastic domains from grain 11 (green spots)  
40  
41 846 and grain 10 (red spots) of this study and the youngest subgroup of Tohver et al. (2012) (green  
42  
43 847 spots). Based on the textural evidence and the concordance of the analyses from grain 11, an impact  
44  
45 848 age of  $262 \pm 9$  Ma is accepted. All error ellipses are  $2\sigma$ .

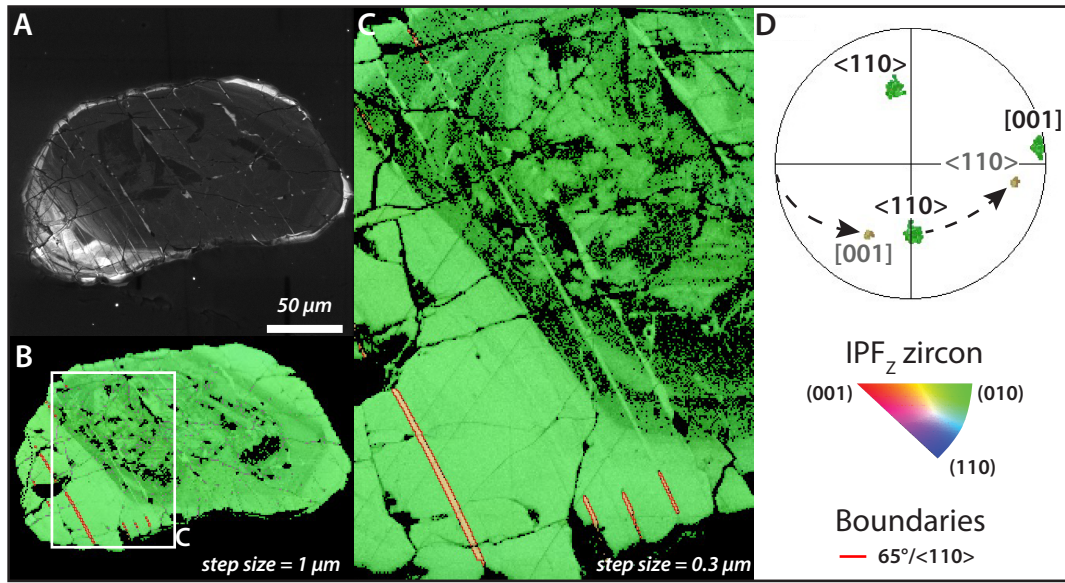
46  
47  
48  
49 849 **Figure 9** Plots of  $^{206}\text{Pb}/^{238}\text{U}$  vs.  $^{208}\text{Pb}/^{232}\text{Th}$  ages for individual analyses from monazite from Vredefort  
50  
51 850 and Araguinha, a 1 to 1 line is plotted as solid grey. A. Variable Pb loss between domains collected  
52  
53 851 from the deformed host and neoblasts from the Vredefort ILG. While the 2020 Ma  $^{207}\text{Pb}/^{206}\text{Pb}$  age is  
54  
55 852 consistent with the Vredefort shock event the U – Th systematics are significantly disturbed post  
56  
57 853 shock, however evenly, either the result of Kibaran regional metamorphism or modern Pb-loss,  
58  
59  
60  
61  
62  
63  
64  
65

1  
2 854 which may have significantly affected the deformed host as well. B. Significant disequilibrium  
3  
4 855 between the U – Th systematics within the deformed host from the Araguainha impact structure,  
5  
6 856 while the systematics of the neoblasts are in agreement with one another, potentially due to the  
7  
8 857 lack of post shock deformation. All error bars are  $2 \sigma$ .  
9  
10  
11  
12  
13  
14  
15  
16  
17  
18  
19  
20  
21  
22  
23  
24  
25  
26  
27  
28  
29  
30  
31  
32  
33  
34  
35  
36  
37  
38  
39  
40  
41  
42  
43  
44  
45  
46  
47  
48  
49  
50  
51  
52  
53  
54  
55  
56  
57  
58  
59  
60  
61  
62  
63  
64  
65

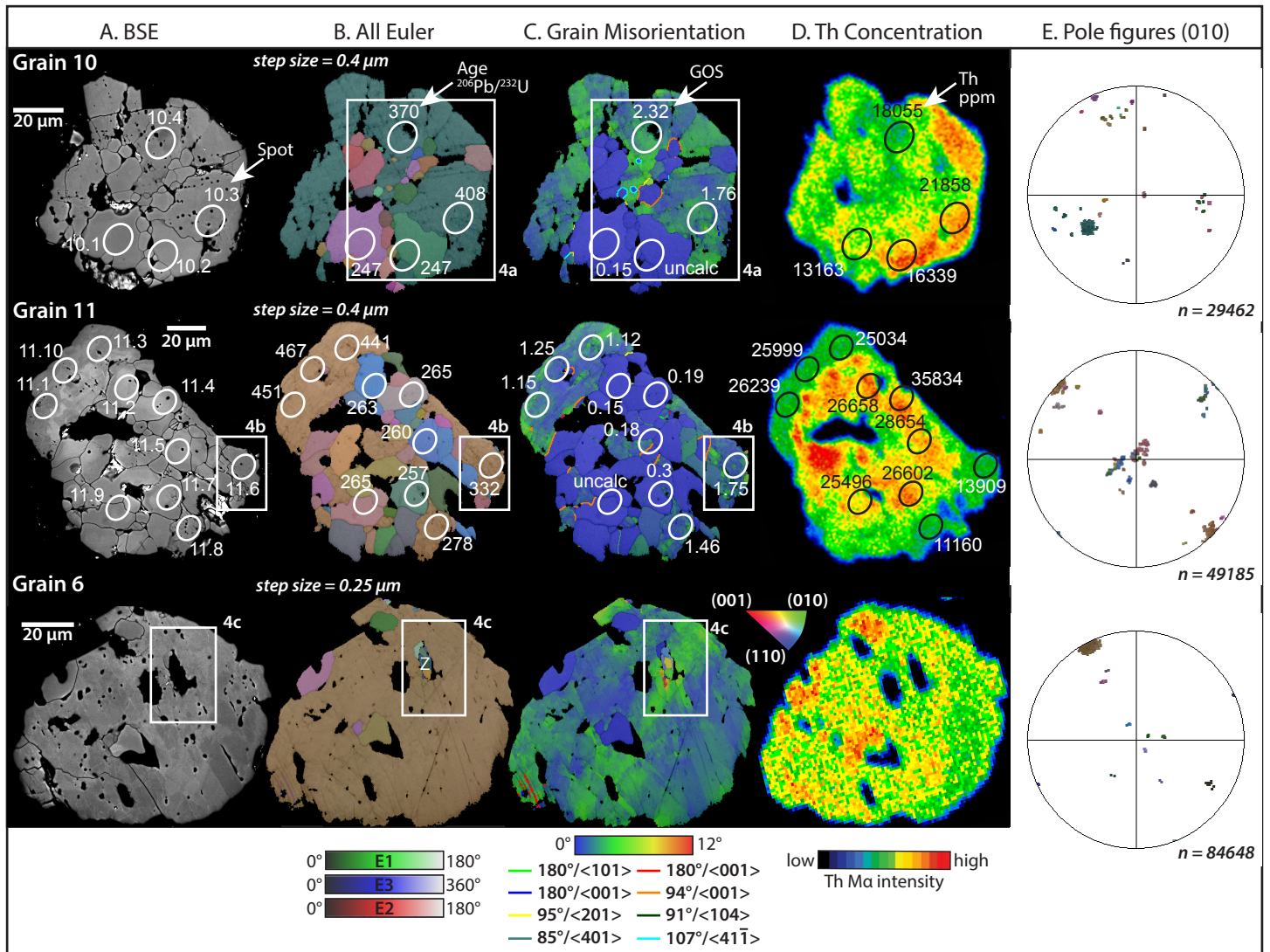




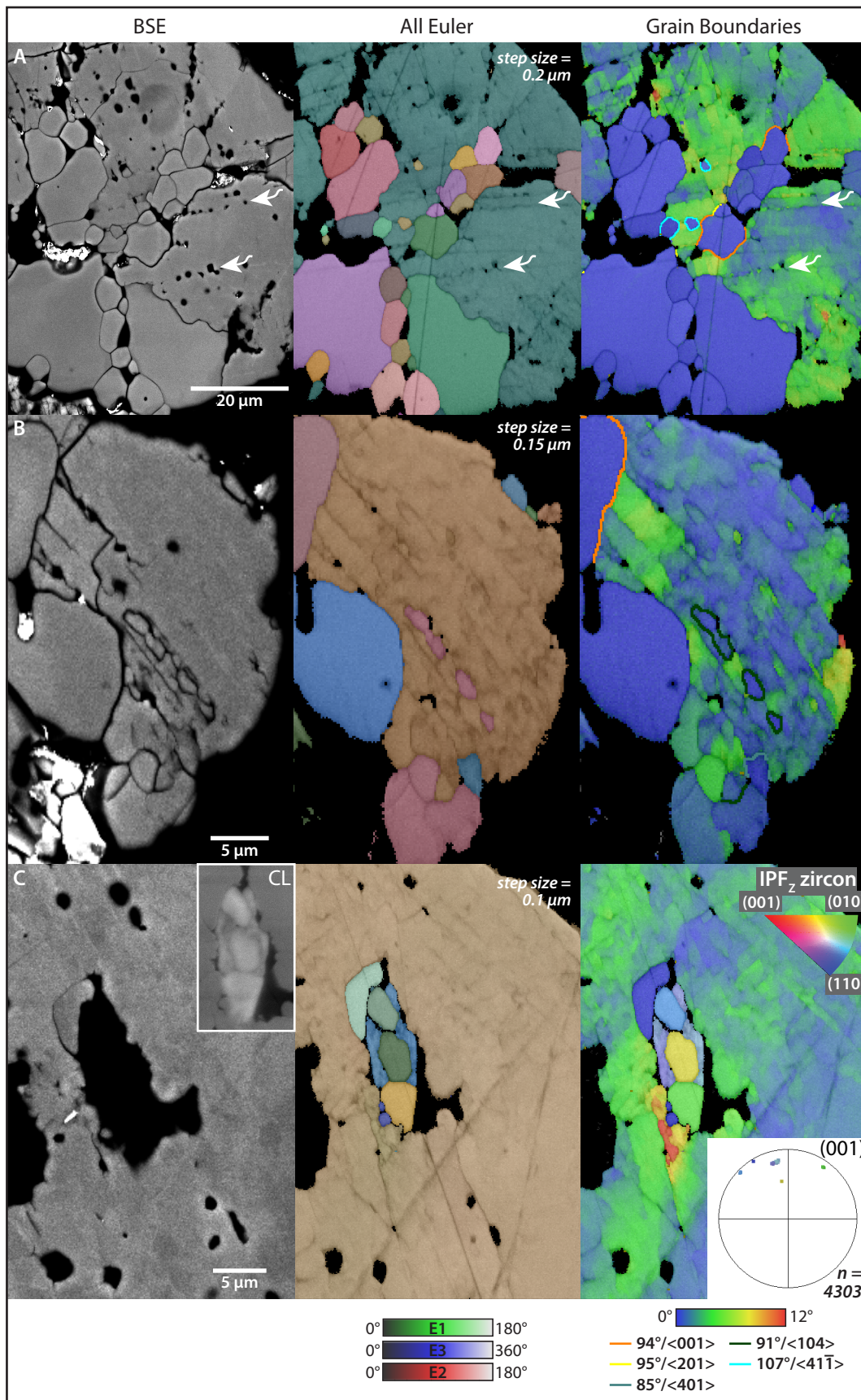
Erickson et al. (2016), Fig. 2





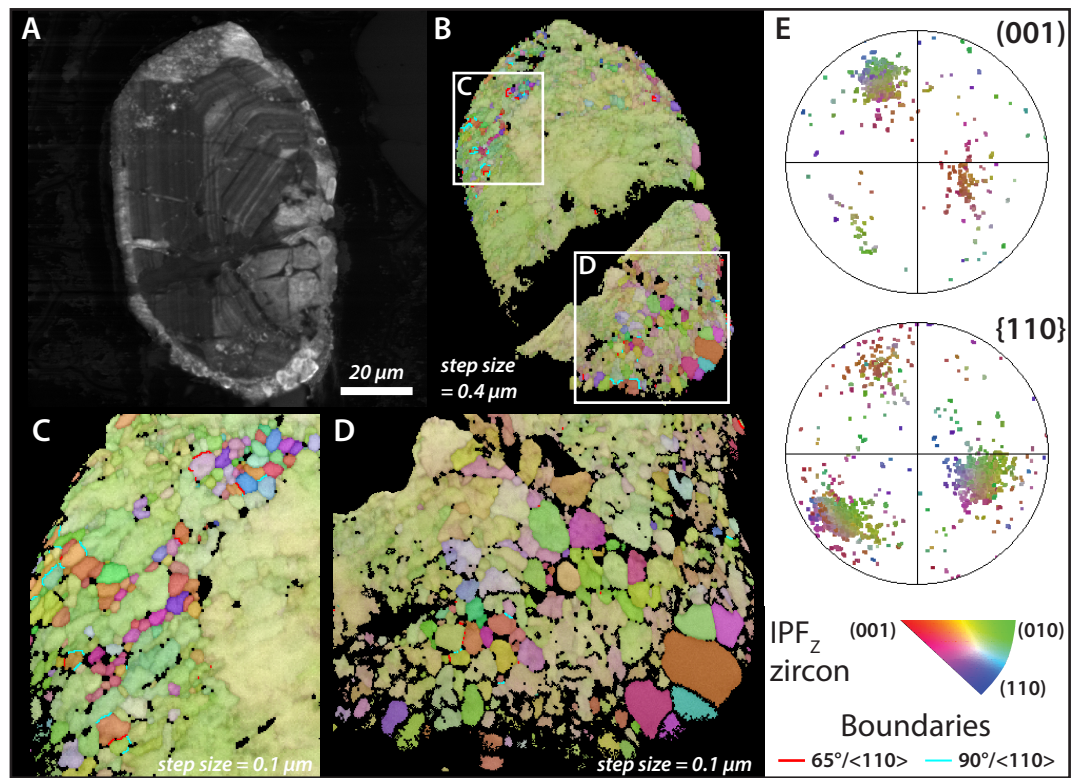


Erickson et al. (2016), Fig. 4

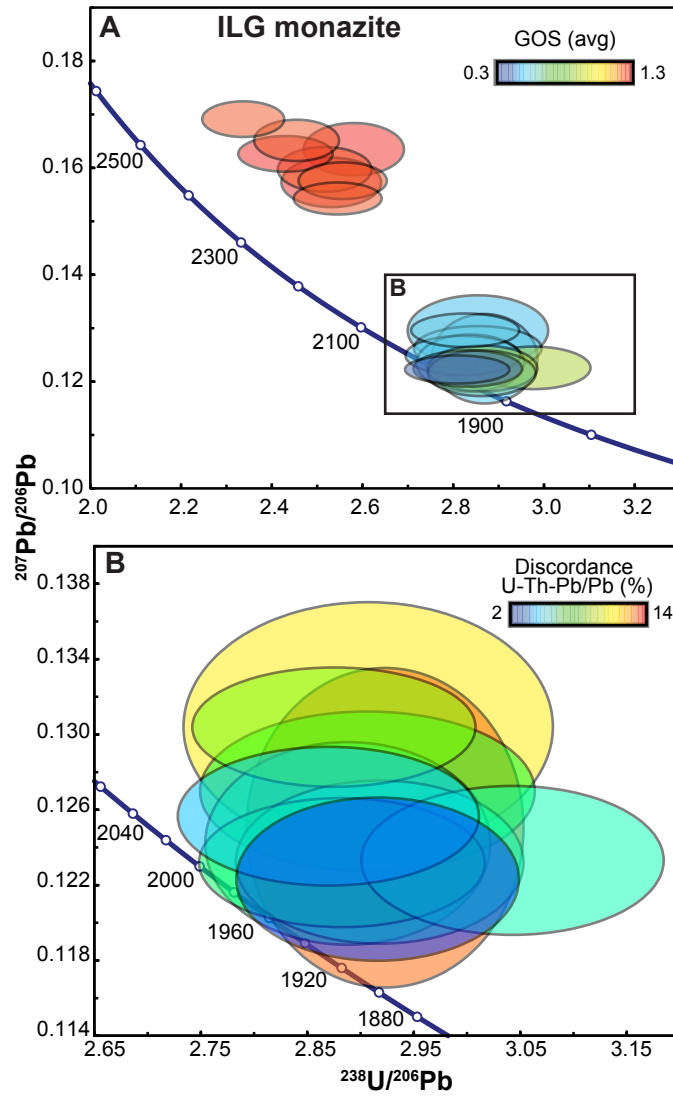


Erickson et al. (2016), Fig. 5

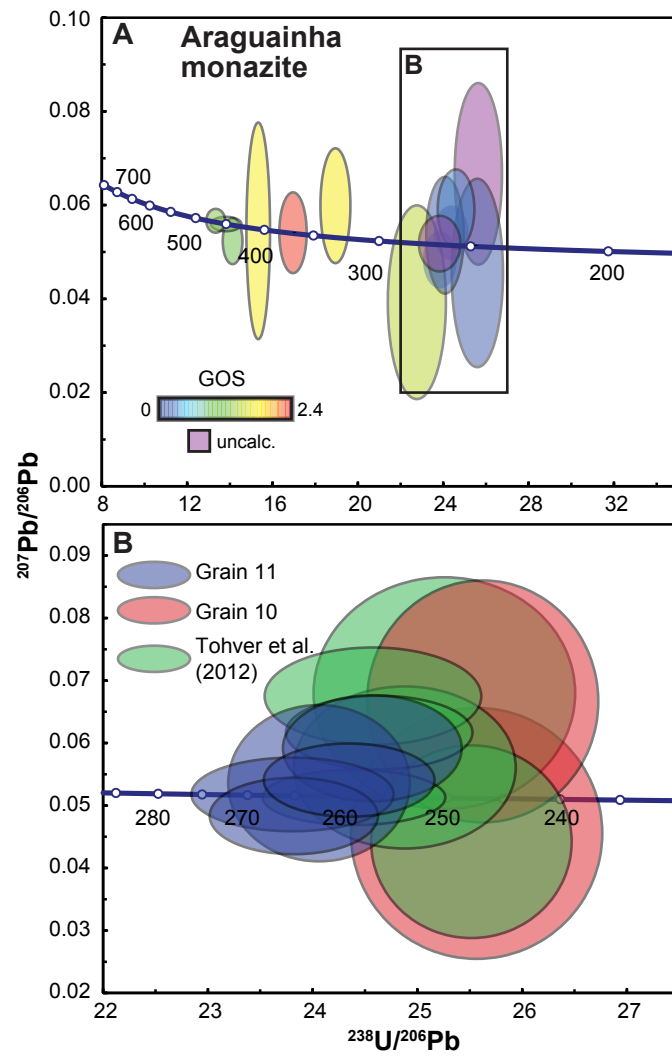




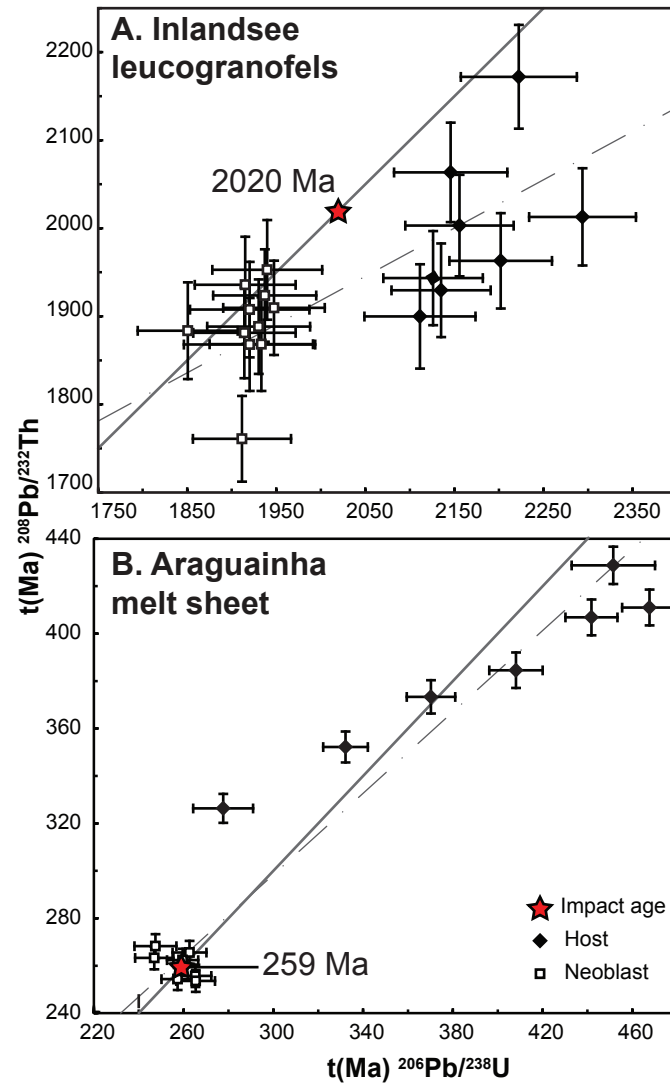
Erickson et al. (2016), Fig. 6



Erickson et al. (2016), Fig. 7



Erickson et al. (2016), Fig. 8



Erickson et al. (2016), Fig. 9

Table 1. SIMS U-Th-Pb analyses for shocked monazite from the Vredefot Inlandsee Leucogranofels (09SA06)

Analytical spot	Domain	U (ppm)	Th (ppm)	Th/U	f <sup>206</sup> Pb %	<sup>208</sup> Pb*/ <sup>232</sup> Th	<sup>207</sup> Pb*/ <sup>235</sup> U	<sup>206</sup> Pb*/ <sup>238</sup> U	<sup>207</sup> Pb*/ <sup>206</sup> Pb	<sup>208</sup> Pb* <sup>‡</sup> Age
09SA06-3.1	Neoblast	584	40937	70.13	-0.08	0.0991 ± 0.0015	5.972 ± 0.116	2.8355 ± 0.0061	0.12280 ± 0.00109	1972
09SA06-3.2	Neoblast	484	27375	56.51	-0.04	0.1005 ± 0.0015	5.822 ± 0.133	2.8909 ± 0.0060	0.12207 ± 0.00180	1950
09SA06-3.3	Neoblast	168	39128	233.14	0.81	0.0968 ± 0.0014	6.234 ± 0.193	2.8824 ± 0.0078	0.13032 ± 0.00276	2009
09SA06-3.4	Neoblast	527	32564	61.78	-0.10	0.0969 ± 0.0014	5.929 ± 0.125	2.8596 ± 0.0062	0.12297 ± 0.00143	1966
09SA06-3.5	Neoblast	551	29345	53.27	1.10	0.0979 ± 0.0015	5.969 ± 0.151	2.8648 ± 0.0061	0.12402 ± 0.00225	1971
09SA06-3.6	Neoblast	358	16590	46.38	0.95	0.1014 ± 0.0015	6.074 ± 0.136	2.8483 ± 0.0066	0.12547 ± 0.00154	1986
09SA06-3.7	Neoblast	234	34673	148.49	0.72	0.0990 ± 0.0015	6.069 ± 0.151	2.8821 ± 0.0071	0.12685 ± 0.00178	1986
09SA06-7.1	Host	686	30451	44.41	2.91	0.0986 ± 0.0016	8.736 ± 0.187	2.5806 ± 0.0068	0.16350 ± 0.00201	2311
09SA06-7.3	Neoblast	202	43912	217.69	0.42	0.0999 ± 0.0014	6.298 ± 0.128	2.8530 ± 0.0062	0.13033 ± 0.00132	2018
09SA06-7.4	Neoblast	176	34251	194.30	-0.88	0.0977 ± 0.0015	5.643 ± 0.126	3.0074 ± 0.0059	0.12309 ± 0.00165	1923
09SA06-7.5	Neoblast	172	31041	180.88	-0.87	0.0975 ± 0.0014	5.863 ± 0.135	2.8925 ± 0.0061	0.12299 ± 0.00181	1956
09SA06-7.6	Host	633	24228	38.26	-0.04	0.1075 ± 0.0015	8.548 ± 0.183	2.5320 ± 0.0070	0.15696 ± 0.00190	2291
09SA06-7.7	Host	754	42479	56.34	0.13	0.1134 ± 0.0016	9.231 ± 0.179	2.4296 ± 0.0072	0.16266 ± 0.00135	2361
09SA06-8.1	Host	1076	31566	29.32	-0.08	0.1042 ± 0.0016	8.708 ± 0.174	2.5183 ± 0.0067	0.15905 ± 0.00171	2308
09SA06-8.2	Host	1109	29338	26.44	-0.09	0.1002 ± 0.0014	8.311 ± 0.145	2.5470 ± 0.0061	0.15352 ± 0.00121	2265
09SA06-8.4	Neoblast	418	36279	86.77	3.58	0.0910 ± 0.0013	5.942 ± 0.196	2.8973 ± 0.0058	0.12486 ± 0.00354	1967
09SA06-8.5	Host	1172	36795	31.39	-0.06	0.1020 ± 0.0015	9.246 ± 0.170	2.4560 ± 0.0064	0.16469 ± 0.00158	2363
09SA06-8.7	Host	791	35763	45.24	-0.14	0.1047 ± 0.0015	9.895 ± 0.175	2.3400 ± 0.0067	0.16794 ± 0.00134	2425
09SA06-8.8	Host	950	30380	31.96	-0.12	0.1009 ± 0.0015	8.436 ± 0.152	2.5596 ± 0.0061	0.15660 ± 0.00140	2279

disc. = discordance; uncalc. = uncalculated

f<sup>206</sup>Pb is the proportion of <sup>206</sup>Pb calculated to be common Pb on the basis of measured <sup>204</sup>Pb/<sup>206</sup>Pb and modelled common Pb composition (Stacey & Kramers, 1975) at th

\*All listed Pb isotope data are corrected for common Pb, based on measured <sup>204</sup>Pb/<sup>206</sup>Pb.

% Discordance<sup>A</sup> calculated as  $[(^{207}\text{Pb}/^{206}\text{Pb}) - (^{206}\text{Pb}/^{238}\text{U})] / (^{206}\text{Pb}/^{238}\text{U}) \times 100$

% Discordance<sup>B</sup> calculated as  $[(^{208}\text{Pb}/^{232}\text{Th}) - (^{206}\text{Pb}/^{238}\text{U})] / (^{206}\text{Pb}/^{238}\text{U}) \times 100$

Listed uncertainties are 1σ.

<sup>‡</sup>Grain orientation spread (avg) calculated from EBSD data, see methods for further details

$^{232}\text{Th}$	$^{206}\text{Pb}^* / ^{238}\text{U}$	$^{207}\text{Pb}^* / ^{206}\text{Pb}^*$			Grain orientation spread (avg)
(Ma)	Age (Ma)	Age (Ma)	% disc. <sup>A</sup>	% disc. <sup>B</sup>	
± 17	1947 ± 28	1997 ± 16	2.6	1.3	0.4
± 20	1915 ± 28	1987 ± 26	3.7	1.8	0.63
± 27	1920 ± 37	2102 ± 37	9.5	4.6	0.47
± 18	1933 ± 29	2000 ± 21	3.4	1.7	0.36
± 22	1930 ± 29	2015 ± 32	4.4	2.1	0.53
± 19	1940 ± 31	2035 ± 22	4.9	2.4	0.49
± 21	1920 ± 34	2055 ± 25	7.0	3.4	0.52
± 19	2111 ± 31	2492 ± 21	18.0	9.5	1.28
± 18	1937 ± 29	2102 ± 18	8.5	4.2	0.52
± 19	1851 ± 28	2002 ± 24	8.2	3.9	0.88
± 20	1914 ± 29	2000 ± 26	4.5	2.2	0.88
± 19	2146 ± 32	2423 ± 20	12.9	6.8	1.28
± 18	2222 ± 33	2484 ± 14	11.8	6.3	1.28
± 18	2156 ± 30	2446 ± 18	13.5	7.1	1.24
± 16	2135 ± 28	2386 ± 13	11.7	6.1	1.24
± 28	1911 ± 28	2027 ± 50	6.0	2.9	0.49
± 17	2202 ± 29	2504 ± 16	13.7	7.3	1.24
± 16	2294 ± 30	2537 ± 13	10.6	5.7	1.24
± 16	2126 ± 28	2419 ± 15	13.8	7.2	1.24

e approximate sample age.

Table 2. SIMS U-Th-Pb analyses for shocked monazite from the Araguinha impact melt (AIM)

Analytical spot	Domain	U (ppm)	Th (ppm)	Th/U	f <sup>206</sup> Pb %	<sup>208</sup> Pb* / <sup>232</sup> Th	<sup>207</sup> Pb* / <sup>235</sup> U	<sup>206</sup> Pb* / <sup>238</sup> U	<sup>207</sup> Pb* / <sup>206</sup> Pb	<sup>208</sup> Pb / Ag <sup>†</sup>
ARA-10.1	Neoblast	335	13163	39.3	9.53	0.01334 ± 0.0001	0.24458 ± 0.043228	0.0391 ± 0.4902	0.04552 ± 0.00820	268
ARA-10.2	Neoblast	225	16339	72.7	9.18	0.01309 ± 0.0001	0.35744 ± 0.039279	0.0390 ± 0.4507	0.06667 ± 0.00791	263
ARA-10.3	Host	1285	21858	17.0	5.63	0.01920 ± 0.0002	0.48867 ± 0.085749	0.0653 ± 0.2300	0.05449 ± 0.00944	384
ARA-10.4	Host	375	18055	48.1	3.18	0.01863 ± 0.0002	0.43894 ± 0.027374	0.0591 ± 0.2542	0.05410 ± 0.00351	373
ARA-11.1	Host	1161	26239	22.6	0.32	0.02144 ± 0.0002	0.55769 ± 0.010637	0.0725 ± 0.2937	0.05602 ± 0.00064	429
ARA-11.2	Neoblast	627	26658	42.5	4.07	0.01320 ± 0.0001	0.30598 ± 0.027238	0.0416 ± 0.3531	0.05359 ± 0.00510	265
ARA-11.3	Host	704	25034	35.6	1.64	0.02033 ± 0.0002	0.50929 ± 0.016449	0.0709 ± 0.1911	0.05232 ± 0.00201	407
ARA-11.4	Neoblast	621	35834	57.7	2.21	0.01271 ± 0.0001	0.27875 ± 0.011426	0.0420 ± 0.3273	0.04834 ± 0.00250	255
ARA-11.5	Neoblast	559	28645	51.3	1.79	0.01304 ± 0.0001	0.30526 ± 0.010204	0.0411 ± 0.3329	0.05411 ± 0.00239	262
ARA-11.6	Host	285	13909	48.7	5.85	0.01757 ± 0.0002	0.43476 ± 0.033228	0.0529 ± 0.2906	0.05990 ± 0.00500	352
ARA-11.7	Neoblast	474	26602	56.1	3.21	0.01264 ± 0.0001	0.33082 ± 0.015563	0.0407 ± 0.3472	0.05917 ± 0.00346	254
ARA-11.8	Host	245	11160	45.6	10.96	0.01626 ± 0.0002	0.23739 ± 0.048583	0.0440 ± 0.5562	0.03929 ± 0.00845	326
ARA-11.9	Neoblast	498	25496	51.2	1.62	0.01260 ± 0.0001	0.29882 ± 0.010357	0.0420 ± 0.3947	0.05179 ± 0.00242	253
ARA-11.10	Host	611	25999	42.5	0.49	0.02054 ± 0.0002	0.58502 ± 0.009420	0.0752 ± 0.1801	0.05666 ± 0.00104	411

disc. = discordance; uncalc. = uncalculated

f<sup>206</sup>Pb is the proportion of <sup>206</sup>Pb calculated to be common Pb on the basis of measured <sup>204</sup>Pb/<sup>206</sup>Pb and modelled common Pb composition (Stacey & Kramers, 1975) at the

\*All listed Pb isotope data are corrected for common Pb, based on measured <sup>204</sup>Pb/<sup>206</sup>Pb.

% Discordance<sup>A</sup> calculated as  $[(^{207}\text{Pb}/^{206}\text{Pb}) - (^{206}\text{Pb}/^{238}\text{U})] / (^{206}\text{Pb}/^{238}\text{U}) \times 100$

% Discordance<sup>B</sup> calculated as  $[(^{208}\text{Pb}/^{232}\text{Th}) - (^{206}\text{Pb}/^{238}\text{U})] / (^{206}\text{Pb}/^{238}\text{U}) \times 100$

Listed uncertainties are 1σ.

† Grain orientation spread calculated from EBSD data, see methods for further details

$^{206}\text{Pb}^*/^{232}\text{Th}$	$^{206}\text{Pb}^*/^{238}\text{U}$	$^{207}\text{Pb}^*/^{206}\text{Pb}^*$	% disc. <sup>A</sup>	% disc. <sup>B</sup>	Grain orientation spread <sup>‡</sup>
± 3	247 ± 5	-28 ± 387	-111.3	8.3	0.15
± 2	247 ± 4	828 ± 230	235.2	6.5	uncalc.
± 4	408 ± 6	391 ± 348	-4.0	-5.7	1.76
± 4	370 ± 5	375 ± 140	1.4	0.9	2.32
± 4	451 ± 9	453 ± 25	0.4	-5.0	1.15
± 2	263 ± 4	354 ± 202	34.8	1.0	0.15
± 4	441 ± 6	299 ± 85	-32.2	-7.9	1.12
± 2	265 ± 4	116 ± 118	-56.2	-3.7	0.19
± 2	260 ± 3	376 ± 97	44.7	0.9	0.18
± 3	332 ± 5	600 ± 171	80.7	6.0	1.75
± 2	257 ± 4	573 ± 122	122.9	-1.3	0.3
± 3	278 ± 7	-397 ± 484	-243.2	17.5	1.46
± 2	265 ± 4	276 ± 103	4.1	-4.6	uncalc.
± 4	467 ± 6	479 ± 40	2.4	-12.1	1.25

<sup>e</sup> approximate sample age.